Chen *et al. Journal of Nanobiotechnology* (2025) 23:364
https://doi.org/10.1186/s12951-025-03349-3

Journal of Nanobiotechnology

RESEARCH **Open Access**

Multi-enzymatic biomimetic cerium-based MOFs mediated precision chemodynamic synergistic antibacteria and tissue repair for MRSA-infected wounds

Shiqi Chen[1†], Yifan Li[2†], Qiang Ma[1], Jiayi Liang[3], Zhiyue Feng[1], Sihan Wang[1,3], Shuai Zhang[1], Ke Han[1], Boyan Sun[1], Hongping Wang[2*] and Haiyang Jiang[1*]

Abstract

Antibiotic-resistant pathogens represent a significant global public health challenge, particularly in refractory infections associated with biofilms. Urgent development of innovative, safe, and therapeutically adaptive strategies to combat these resistant biofilms is essential. We present a novel biomimetic antibacterial system inspired by the multifunctional enzymatic properties of cerium-based metal–organic frameworks. This system utilizes the inherent oxidase and peroxidase activities of a nanozyme to generate reactive oxygen species (ROS) for bacterial eradication, while its phosphate-ester hydrolase activity disrupts bacterial genetic material and energy metabolism. By the reversible covalent binding between boronic acid groups and cis-diol groups on bacterial surfaces, combined with abundant cerium catalytic sites from the porous structure and the potent antibacterial effects of sanguinarine, we enhance targeted antibacterial activity. This system effectively penetrates extracellular polymeric substances (EPS) and demonstrates precise regulation of ROS, allowing for localized delivery of ROS and sanguinarine for biofilm eradication. Transcriptomic analyses indicate that this approach disrupts the cellular environment, impairs energy metabolism, inhibits bacterial attachment to EPS, and promotes biofilm dispersion by modulating drug resistance-related genes. In vivo experiments confirm that this nanocatalyst composite effectively treats biofilm-induced wounds with efficacy comparable to vancomycin, presenting a promising solution for managing chronic infections caused by antibiotic-resistant biofilms.

Highlights

1. Cerium-based functional multi-enzymatic biomimetic antibacterial system was developed for the first time.
2. The system facilitate controlled ROS regulation, localized delivery and biofilm eradication.
3. The system modulats drug resistance and biosynthesis for biofilm eradication.

[†] Shiqi Chen and Yifan Li have contributed equally to this work.

*Correspondence:
Hongping Wang
wanghp@scidc.org.cn
Haiyang Jiang
haiyang@cau.edu.cn
Full list of author information is available at the end of the article

4. The system effectively treats infected wounds comparable to vancomycin.

Keywords Antibacteria, Nanozymes, Targeted delivery systems, MRSA, Infected wound healing

Graphical Abstract

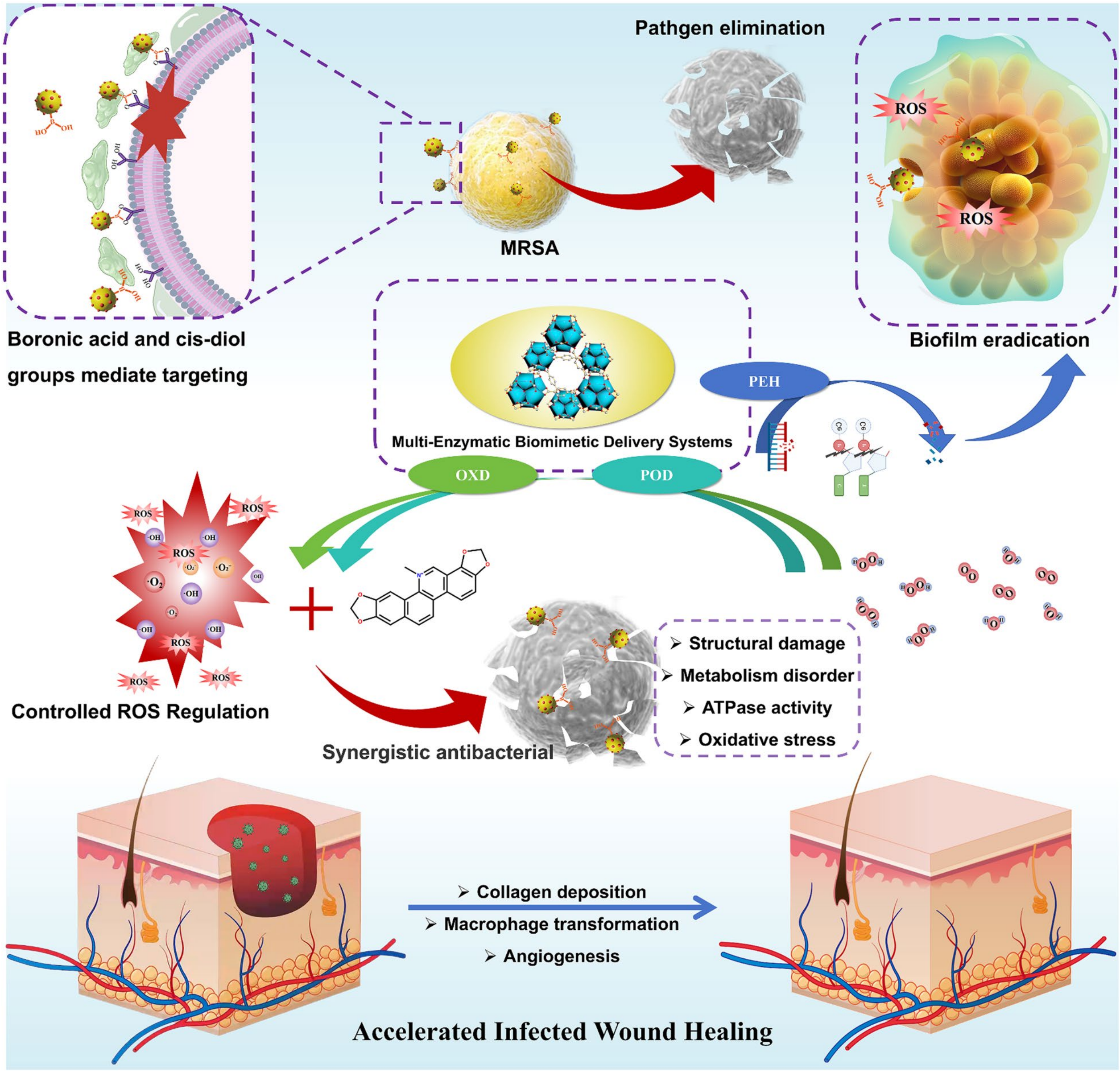

Introduction

Bacterial infection afflicts millions of people and animals annually worldwide, causing a severe threat to public health [1]. *Staphylococcus aureus* is a multifaceted pathogen, capable of causing a wide range of diseases, from relatively minor skin and soft tissue infections to invasive, life threatening infections including bacteremia and sepsis [2]. The emergence of antibiotics greatly relieved the pain of infected patients, however, *S. aureus* antibiotic resistance continues to increase, as evidenced by the large number of methicillin-resistant *S. aureus* (MRSA) infections [3]. Even worse, the exploitation of novel antibiotics lags behind the growth of drug resistance [4]. MRSA-infected wound is a common and complex clinical issue that causes significant health burdens and medical challenges globally, dramatically escalating morbidity and mortality [5, 6]. Notably, ≈ 80% of MRSA wound infections are stubborn, refractory, and frequently complicated, which are highly susceptible to biofilm formation, preventing antibiotics from penetrating and clearing the infection [7, 8]. In contrast to planktonic bacteria, biofilms are characterized by a robust extracellular polymeric substance (EPS) matrix, which consists of extracellular DNA (eDNA), polysaccharides, lipids, and proteins [9, 10]. This matrix, combined with a biofilm microenvironment (BME) that is rich in acidity and hydrogen peroxide (H_2O_2), effectively shields the bacteria from host immune defenses and hinders the penetration of antibacterial agents [11, 12]. Thus rendering great challenges to the current antibacterial therapies. Therefore, finding an effective therapeutic strategy to address biofilm infections has become one of the current challenges.

Chemodynamic therapy (CDT), which utilizes Fenton or Fenton-like reactions to generate reactive oxygen species (ROS) in situ, was first proposed by Bu's group for cancer treatment [13, 14]. Recently, CDT has also been extensively studied as an alternative treatment for antibiotic-resistant infections [15, 16]. Stable ROS generation is crucial for enhancing the efficiency of CDT [17]. Artificial nanozymes have emerged as promising biocatalysts for this purpose due to their straightforward synthesis and stable performance [18]. Among these, oxidoreductase-like nanozymes are predominant, comprising 96% of all nanozymes [19, 20]. These nanozymes can generate ROS that effectively targets and disrupt biofilms, bacterial membranes, nucleic acids, and proteins at acidic infection sites, leading to bacterial inactivation [21]. Encouragingly, the bactericidal strategy utilizing nanozymes for ROS production significantly mitigates the risk of developing drug resistance compared to traditional antibiotics [22]. Cerium, the most abundant rare-earth metal and the most reactive element in the lanthanide series, is widely utilized in catalyst production [23]. Cerium-based nanozymes have demonstrated diverse mimetic enzyme activities, including oxidase, peroxidase, catalase, and phosphatase [24]. Notably, their unique phosphatase activity facilitates the cleavage of eDNA within the EPS matrix, thereby enhancing biofilm clearance and increasing the efficacy of bacterial eradication [25, 26]. The versatility of cerium-based nanozymes significantly improves their effectiveness in complex BME, specifically in targeting and eliminating bacteria shielded by EPS [27, 28]. Therefore, cerium presents an ideal element for constructing multi-enzyme catalytic systems tailored to meet antimicrobial requirements.

In addition to the constituent elements, a sufficient abundance of catalytic sites and adequate contact between these sites and substrates are critical factors for ensuring efficient catalytic activity [29, 30]. Metal–organic framework (MOF)-based nanozymes and their derivatives have emerged as promising candidates to fulfill these requirements [31, 32]. Distinguished by their well-defined coordination networks, mesoporous structures, and tunable pore size distributions, these materials feature controllable cavities and channels that create hydrophobic coordination environments similar to those found in natural enzymes, thereby establishing them as some of the most promising nanoenzymes available [33, 34]. Furthermore, cerium can be utilized to construct nano-sized cerium (Ce) MOF, specifically Uio-66 (Ce), as demonstrated in previous studies [35, 36]. This versatility significantly enhances the potential for developing efficient multi-catalytic systems and controlled ROS regulators [37]. To further improve the anti-MRSA activity of these biocatalytic systems, sanguinarine (SA), extracted from the medicinal herb *Macleaya cordata*, was loaded into Uio-66 (Ce). Notably, the antibacterial activity of SA exceeds that of the well-known natural antibacterial agent berberine [38]. Due to its remarkable bacteriostatic effects, affordability, and accessibility, SA has found widespread application in veterinary medicine, animal feed additives, and antibacterial toothpaste [39]. Leveraging the reversible covalent interactions between boronic acid (BA) moieties and cis-diols, which facilitate the formation of five- or six-membered cyclic borate ester complexes, BA has emerged as a promising receptor for targeting pathogenic bacteria [40, 41]. Specifically, MRSA can be effectively captured through boronate affinity, capitalizing on the abundant binding sites provided by the high concentration of peptidoglycans and teichoic acids present on the bacterial surface [42]. Moreover, boronate-mediated targeting systems demonstrate significant advantages over traditional recognition elements in terms of cost-effectiveness and rapid association kinetics.

Considering the aforementioned factors, an innovative multi-enzyme activity and bacteria-targeted SA/B-Uio-66 (Ce) composite, consisting of B-Uio-66 (Ce) and SA, was designed and fabricated for the treatment of drug-resistant infections and promotion of cutaneous regeneration through a "controlled ROS regulation" approach in this study. The SA/B-Uio-66 (Ce) composites were synthesized using post-synthetic modification techniques following the initial solvothermal synthesis [43]. The incorporation of SA/B-Uio-66 (Ce) enables the efficient catalytic generation of ROS and, in combination with synergistic natural antibacterial agents, targets and directly eradicates planktonic MRSA in the early stages of infection(Scheme 1) [44, 45]. Systematic in vitro studies demonstrate that BA modification is crucial for bacterial capture. The multi-enzyme activity (oxidase (OXD)-, peroxidase (POD)-, and phosphate-ester hydrolase (PEH)-mimetic) of B-Uio-66 (Ce) significantly contributes to biofilm penetration and eradication, which eventually induces hole structures to facilitate in situ ROS delivery and enhances biofilm eradication. Extensive assessments of cytocompatibility and wound healing capabilities were conducted through in vitro and in vivo investigations, effectively showcasing the remarkable potential of this targeted nanocatalytic system to address the challenges associated with treating persistent bacteria-invaded wounds and advancing the field of therapeutic wound dressing technology.

Materials and methods

Materials

Ammonium ceric nitrate ($(NH_4)_2Ce(NO_3)_6$), p-Phthalic acid (PTA), 4-Aminophenylboronic acid (4-APBA), 3,3,5,5-tetramethylbenzidine (TMB), Methylene blue (MB), Bis-(4-nitrophenyl) phosphate (BNPP), 1,3-Diphenylisobenzofuran (DPBF) were purchased from Macklin reagents (Shanghai, China), Sanguinarine (SA) was obtained from Yuanye Bio-Technology Co., Ltd (Shanghai, China). Cell lines (L929) and culture reagents were purchased from Wuhan Pricella Biotechnology Co., Ltd. All other chemicals were used as received without further purification, and deionized pure water (18.2 MΩ·cm) used in the experiments was produced from a Milli-Q Academic system (Millipore Co., Ltd, USA).

Synthesis of Uio-66 (Ce)

The synthesis schemes were partially adjusted based on the previous reports [36, 46]. In brief, $(NH_4)_2Ce(NO_3)_6$ (1.17 g, 2.135 mmol), acetic acid (122 μL), and PTA (0.355 g, 2.135 mmol) were dispersed in 23 mL 80% aqueous DMF solution. After heating at 100 °C for 15 min, the white UiO-66 (Ce) was collected and washed three times with DMF. To expose adsorption and catalytic sites, the solid was then dried at 70 °C overnight and later under vacuum.

Synthesis of B-Uio-66 (Ce)

The 50 mg Uio-66 (Ce), EDC and NHS were dispersed in 12 mL of ultra-pure water, and the mixture was stirred at 0 °C for 2 h. Then, 100 mg of 4-APBA was added to react overnight. After the reaction, the solution was dialyzed using a 3500 Da molecular weight cutoff membrane for 24 h. The resulting yellow B-Uio-66 (Ce) solid powder was collected by centrifugation and freeze-drying.

Synthesis of SA/B-Uio-66 (Ce)

Following the successful preparation of B-Uio-66 (Ce), the powder was dispersed in ethanol containing 1 mg/mL sanguinarine and shaken overnight in the dark at room temperature. After the incubation period, the mixture was centrifuged at 10,000×*g* for 10 min to collect the powder. The collected powder was then washed with ethanol three times, followed by another round of centrifugation at 10,000×*g* for 10 min. The final product was obtained by freeze-drying and stored in a refrigerator at 4 °C.

Characterization of SA/B-Uio-66 (Ce)

The general structures of the SA/B-Uio-66 (Ce) and the interaction with MRSA were identified through SEM (SU8020, HITACHI, Japan). TEM (Tecnai G2 F30, FEL, USA) incorporating EDS (Xplore, Oxford, USA) was applied to examine the element proportion and microstructure of the SA/B-Uio-66 (Ce) and bacterial. XRD (D8 Focus, Bruker, Germany) was applied to investigate the phase components of materials. The surface chemistry of materials was examined via XPS (ESCALAB 250XI equipment, Thermo, USA) and FTIR (Nicolet 6700, Thermo, USA). The diameter and zeta potential of these products were measured with a dynamic light scattering (DLS) instrument (NanoZS, Marven, UK) at room temperature. The textural properties of surface areas were determined from the Brunauer–Emmett–Teller (BET) method (ASAP 2460, Micromeritics, USA). The absorption spectra were measured by an ultraviolet–visible-near infrared (UV–vis-NIR) spectrophotometer (UV-3600, Shimadzu, Japan). To assess the thermal stability and thermal degradation of Uio-66 (Ce), B-Uio-66 (Ce) and SA/B-Uio-66 (Ce), a thorough thermal analysis was conducted utilizing a thermogravimetric analyzer (TGA, Mettler TGA2 Switzerland) with a temperature range from 25 to 900 °C and a heating rate of 10 °C/min.

Assessment of OXD-mimetic activity

The OXD activity was rigorously assessed by meticulously adapting and refining the standard protocol for

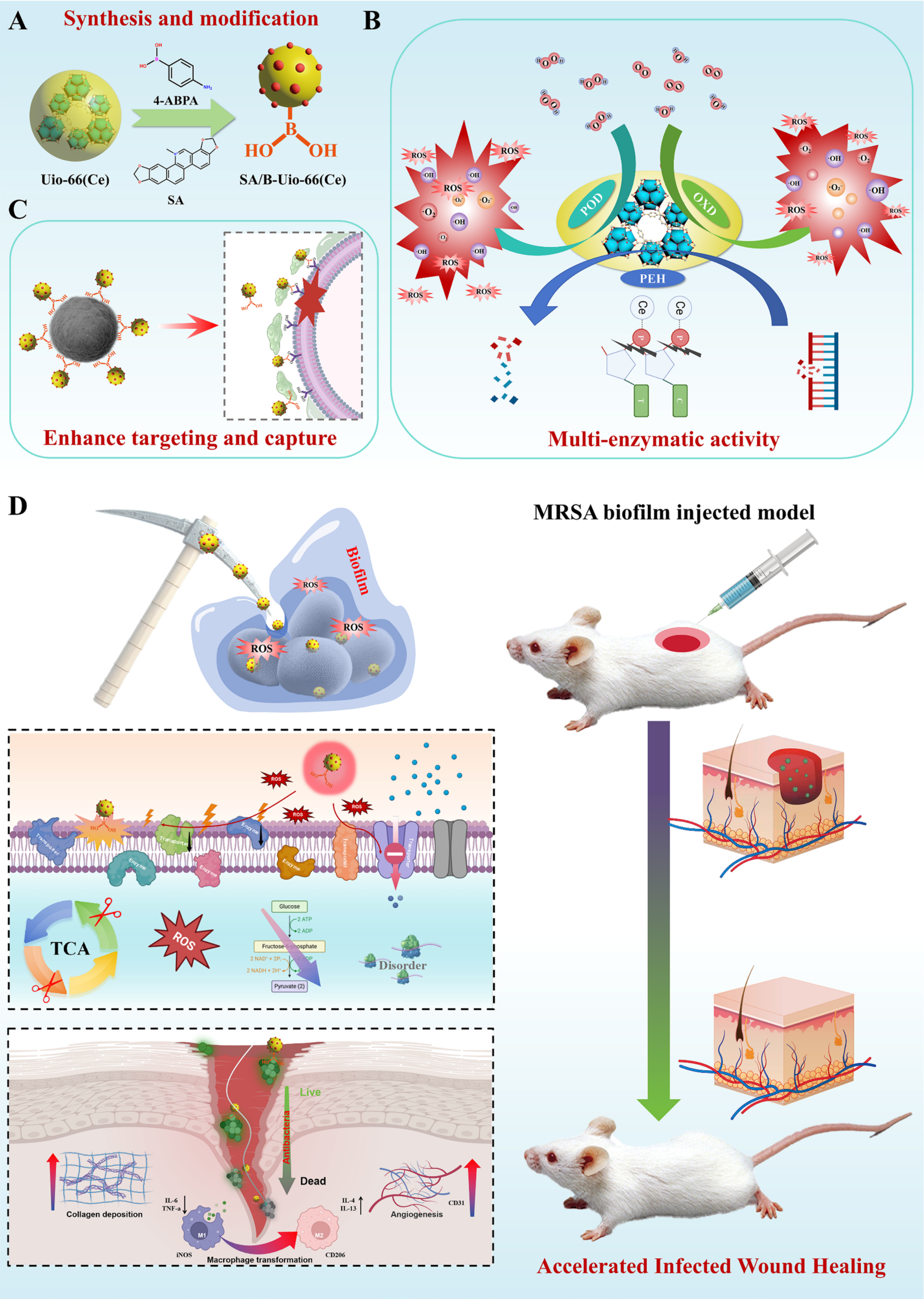

Scheme 1 Schematic illustration of **A** the facile synthesis of multi-enzymatic & targeted biomimetic system, **B** the multi-enzymatic (oxidase (OXD)-, peroxidase (POD)-, and phosphate-ester hydrolase (PEH)-mimetic) activity of system, **C** the targeted delivery based on dynamic borate ester bond, and **D** the application for efficient biofilm eradication and infected wound healing

evaluating nanozyme peroxidase-like catalytic activity [47]. The experimental setup involved the preparation of a 96-well plate, where each well received 180 μL of TMB solution (0.5 mg/mL) and 20 μL of a 0.2 M NaAc/HAc buffer (pH 3.6). Subsequently, a gradient of SA/B-Uio-66 (Ce) concentrations, ranging from 0 to 10 μg, was introduced into the respective wells. A control well, devoid of TMB, was also included to establish a baseline for background measurements. The mixtures were then incubated at 37 °C to emulate physiological conditions under dark conditions, and the colorimetric response was continuously monitored by recording the absorbance at 652 nm at 10-s intervals over a 400-s period after TMB addition. Post-reaction, DLS was employed to ascertain the stability and size distribution of the nanozymes within the reaction medium. The resulting absorbance data were corrected by subtracting the background absorbance attributable to the nanoparticles themselves, and the corrected values were plotted against reaction time to generate the kinetic profile. The catalytic activity was quantified and the specific activity was calculated by using the following formulas:

$$\text{bnanozyme} = \frac{\text{V}}{(\varepsilon \times \text{L})} \times \left(\frac{\Delta\text{A}}{\Delta\text{T}}\right)$$

$$\text{ananozyme} = \frac{\text{bnanozyme}}{[\text{m}]}$$

where $b_{nanozyme}$ is the catalytic activity of nanozyme expressed in units. One unit is defined as the amount of nanozyme that catalytically produces 1 μmoL of product per min at 37 °C; V is the total volume of reaction solution (200 μL); ε is the molar absorption coefficient of the colorimetric substrate, which is typically maximized at 39,000/M cm at 652 nm for TMB; L is the path length of light traveling in the well (0.6 cm); A is the absorbance after subtraction of the blank value; and $\Delta A/\Delta t$ is the initial rate of change in absorbance at 652 nm per min; $a_{nanozyme}$ is the specific activity expressed in units per milligram (U/mg) nanozymes; and [m] is the nanozyme weight (mg) of each assay.

Assessment of POD-mimetic activity

Similarly, following the systematic approach established in previous studies to evaluate the material's POD activity [47]. Specifically, a defined amount of H_2O_2 was added to the reaction mixture to achieve a final concentration of 50 μM under the same conditions used for the OXD activity assessment. The remainder of the process was identical to the OXD activity evaluation, ensuring consistency in the experimental setup.

Steady-state enzyme kinetic studies

The catalytic kinetics were meticulously investigated by introducing a gradient of TMB concentrations (ranging from 0 to 2.8 mM) into the reaction mixture within a 0.2 M NaAc/HAc buffer at pH 3.6, across various wells. The samples were thoroughly mixed and incubated in a 37 °C water bath, where the initial rate of absorbance change at 652 nm was continuously monitored. DLS was concurrently employed to assess the stability and size distribution of the nanozymes during the reaction. The observed rates of absorbance increase were converted to substrate consumption rates, expressed in micromoles per minute, and plotted against the corresponding substrate concentrations to generate a Michaelis–Menten curve. The kinetic constants, v_{max} (maximum reaction velocity) and K_m (Michaelis constant) were determined by fitting the experimental reaction velocity values and substrate concentrations to the Michaelis–Menten equation:

$$\text{v} = \frac{\text{vmax} \times [S]}{K\text{m} + [\text{S}]}$$

where v is the initial reaction velocity and v_{max} is the maximal reaction rate that is observed at saturating substrate concentrations. [S] is the concentration of the substrate and K_m is the Michaelis constant. K_m reflects the affinity of the nanozyme for its substrate and is defined as the substrate concentration at half the maximum rate.

Assessment of phosphatase-mimetic activity

The catalytic hydrolysis rate of BNPP was evaluated using the initial slope method at 25 °C in a Tris buffer solution (pH 8.0), based on the absorbance of BNPP at 400 nm. The release of NP was quantified by measuring the absorbance of the supernatant at 400 nm using a microplate reader and calculating the amount of NP released according to the calibration curve of nitrophenolate at 400 nm. The reaction system comprised 1.0 mg/mL of nanomaterial, 0–3 mM BNPP, and 50 mM Tris buffer. Kinetic data were obtained using the initial slope method (product conversion rate of 5%). The pseudo-first-order rate constant, Kobs (s-1), was determined based on the initial rate slope and BNPP concentration. Background interference from all samples without materials was subtracted. The K_m and v_{max}, were derived using the Lineweaver–Burk equation:

$$\frac{1}{\text{v}} = \frac{K\text{m}}{[S] \times \text{vmax}} + \frac{1}{\text{vmax}}$$

where the meanings of the parameters are consistent with those in sect. "Assessment of OXD-mimetic activity".

Detection of hydroxyl radical (·OH)

MB was employed as a trapping agent to qualitatively assess the production of hydroxyl radicals (·OH) by these materials. The experiment involved placing the material on a 96-well plate, followed by the addition of 200 μL of an acetic acid/sodium acetate (HAc/NaAc) buffer solution containing 5 μg/mL of MB. The absorption spectra of MB were subsequently recorded using a UV–vis spectrophotometer integrated with a microplate reader. Furthermore, the generation of ·OH radicals was analyzed using electron paramagnetic resonance (EPR) spectroscopy with 5,5-dimethyl-1-pyrroline N-oxide (DMPO) as the spin-trapping agent in a DMSO solvent. In this process, 100 μL of biocatalysts (concentration: 10 mg/mL in H_2O) was mixed with 100 μL of a DMPO solution at a concentration of 100 mM.

Detection of singlet oxygen and superoxide anion ($^1O_2$/$O_2^{\cdot -}$)

To detect the singlet oxygen ($^1O_2$) generated by the material under investigation, DPBF was employed as the $^1O_2$ trapping agent. The DPBF solution was prepared by diluting a 25 mM stock to 50 μM using deionized water. After placing the material in a 96-well plate, 200 μL of the DPBF solution was added. The absorption spectra of the DPBF solution were then measured using a microplate reader. The generation of superoxide anions ($O_2^{\cdot -}$) was assessed via EPR spectroscopy, using DMPO as the spin-trapping agent in a DMSO solvent. This involved combining 100 μL of a biocatalyst solution (at 10 mg/mL in H_2O) with 0.05 mL of methanol and 100 μL of a DMPO solution at a 100 mM concentration. Additionally, the generation of $O_2^{\cdot -}$ was evaluated using EPR spectroscopy with 2,2,6,6-tetramethylpiperidine-1-oxyl (TEMP) as the spin-trapping agent in a sodium acetate-acetic acid buffer (100 mM, pH 4.5). For this evaluation, 100 μL of the biocatalyst (10 mg/mL in NaOAc-HOAc buffer) was mixed with 100 μL of a TEMP solution at a 100 mM concentration.

Assessment of scavenge activity of H_2O_2

The scavenge of H_2O_2 was evaluated by EPR spectrometer using 3-carbamoyl-2,2,5,5-tetra-methyl-3-pyrroline-1-yloxyl (CTPO) spin-trapping adduct. In a control group, 400 μL of a 20 mM hydrogen peroxide solution and 100 μL of deionized water were added to 500 μL of a 100 mM CTPO solution. The mixture was deoxygenated for 30 min. For the experimental group, 100 μL of a sample solution at a concentration of 500 μg/mL replaced the deionized water.

Antibacterial properties in vitro

Methicillin-resistant *Staphylococcus aureus* (MRSA, ATCC 33591, Gram-positive) was employed as a representative pathogenic bacterium to evaluate the bacterial capture and eradication capabilities of the SA/B-Uio-66 (Ce) catalytic and targeted systems. The bacteriostatic properties were assessed through minimum inhibitory concentration (MIC) values, agar plate counting, and absorbance measurements at 600 nm (OD_{600}).

For further assessment, bacterial suspension (10^6 CFU/mL) was cultured at 37 °C for 24 h. OD_{600} values of the bacterial suspensions treated with 250 μg/mL of biocatalysts or 0.625 μg/mL of SA were recorded hourly to monitor bacterial growth. The antibacterial properties were evaluated by comparing the OD_{600} values of the treated systems with those of the control.

The bactericidal performance and bacterial capture ability of these systems were visualized using SEM, TEM, and EDS. After treatment with the different systems, the bacterial suspensions were fixed with 2.5 wt% glutaraldehyde and dehydrated through a gradient series of ethanol/water solutions. Subsequently, images were obtained to assess the material's targeting ability and to observe bacterial morphologies.

Bacteriological suspension (1×10^6 CFU/mL) was cultured with various materials lasting 6 h at 37 °C with continual shaking. Following that, the materials were rinsed several times with PBS. Each well received a 200 μL colored combination of SYTO 9 and propidium iodide (PI), and was stained lasting 15 min using the LIVE/DEAD staining kit (Maokang Biotechnology Co., Ltd). Microbes in every group were photographed using Leica SP 8 WLL Confocal Laser Scanning Microscope (CLSM) after staining. 3,3′-Dipropylthiadicarbocyanine iodide ($DiSC_3(5)$, Maokang Biotechnology Co., Ltd) was used to determine the dissipated membrane potential of MRSA after different treatments, after which the fluorescence intensity was recorded using ImageJ. In addition, a mixture of bacteria from the five groups was treated with a 2, 7 dichlorodihydrofluorescein diacetate (DCFH-DA) probe and incubated for 20 min in an oven at 37 ℃. After incubation, the solutions were washed three times with PBS, and green fluorescence was detected via CLSM. Then, images were taken and recorded, and the images were processed using ImageJ.

To evaluate the disruption of the biofilm by the material, 100 μL of cultivated MRSA suspensions at a concentration of 1×10^6 CFU/mL and 900 μL of TSB were added to a 6-well plate and incubated at 37 °C for 24 h to form a complete biofilm. The biofilms were then treated with PBS, SA/B-Uio-66 (Ce), B-Uio-66 (Ce), Uio-66 (Ce), and SA, and the mixtures were incubated at 37 °C for another 24 h. After incubation, the supernatant was removed, and the biofilms at the bottom were washed three times with PBS (pH 7.4). Subsequently, the biofilms were processed using crystal violet staining and quantitatively analyzed using a UV–vis detector.

Additionally, the five groups were stained with SYTO-9 and PI for 30 min at room temperature and imaged using confocal laser scanning microscopy (CLSM) to obtain three-dimensional fluorescence images. To investigate the material's inhibition of the biofilm, 100 μL of MRSA was added to each of the five solutions: PBS, SA/B-Uio-66 (Ce), B-Uio-66 (Ce), Uio-66 (Ce), and SA. The mixed solutions were co-incubated at 37 °C for 48 h. Following the methods used in the biofilm disruption assay, the five groups were subjected to crystal violet staining for quantitative analysis using a UV–vis detector, and three-dimensional fluorescence images were obtained via CLSM using live-dead staining. Biofilm three-dimensional reconstruction and volume calculation were performed using IMARIS Bitplane imaging software.

Transcriptome analysis

MRSA was collected following treatment of SA/B-Uio-66 (Ce), and three independently produced mRNA samples from each condition were utilized for mRNA sequencing. Post-treatment with SA/B-Uio-66 (Ce), an investigation into the gene expression patterns of MRSA was undertaken. This analysis encompassed the utilization of Illumina sequencing technology, involving the Illumina TruSeq mRNA sample prep kit and HiSeq 4000 SBS kit (Illumina, Inc.). This approach made use of the Genome Database for mRNA sequencing analysis.

Biocompatibility evaluation

L929 (2×10^5 cells/well) were seeded in 96-well plates and cultured overnight at 37 °C. The following day, samples (PBS, SA/B-Uio-66 (Ce), B-Uio-66 (Ce), Uio-66 (Ce), and SA) were added to each well and co-incubated for 1, 3 and 7 days. Subsequently, the medium was replaced with 110 μL of a CCK-8 solution. After 2 h of incubation, the absorbance of the samples at 450 nm was measured using a microplate reader.

For fluorescence imaging, L929 (2×10^5 cells/well) were seeded in 6-well plates and cultured overnight at 37 °C. The following day, samples (PBS, SA/B-Uio-66 (Ce), B-Uio-66 (Ce), Uio-66 (Ce), and SA) were added to each well and co-incubated for 1, 3, and 7 days. Live/Dead staining was performed as previously described. After co-incubation, treated cells were stained with Calcein (live cells, green) and PI (dead cells, red) for 30 min. The cells were then immediately visualized using fluorescence microscopy.

Fresh mouse blood was centrifuged at 3500 rpm for 5 min to isolate red blood cells (RBCs) from the serum. The RBCs were then washed with PBS solution until the supernatant was clear. Subsequently, different treatments were applied to the RBCs: negative control group (PBS), positive control group (Triton-X 100), and several trial groups (SA/B-Uio-66 (Ce), B-Uio-66 (Ce), Uio-66 (Ce), and SA) with various concentrations. These samples were gently mixed and incubated in a 37 °C water bath for 4 h, followed by centrifugation. The optical density (OD) of the samples was measured at 540 nm using a microplate reader. The hemolysis ratio was calculated using the following formula:

$$\text{Hemolysis }(\%\,) = \left(\frac{\mathrm{ODx} - \mathrm{OD0}}{OD\mathrm{y} - OD0}\right) \times 100\%$$

where OD_x is the value of the trial sample, OD_0 is the value of the negative control (untreated RBCs), and OD_y is the value of the value of the positive control (RBCs treated with 0.1% Triton X).

To evaluate the in vivo biosafety, healthy mice received a single intraperitoneal injection of samples, including PBS (negative control), SA/B-Uio-66 (Ce), B-Uio-66 (Ce), Uio-66 (Ce), and SA. After 24 h, routine blood examinations and blood biochemistry analyses were performed. Additionally, histological observation of major viscera in the SA/B-Uio-66 (Ce) group was conducted using histological hematoxylin–eosin (H&E) staining.

Evaluation of infected wound healing

All the animal studies followed the animal ethical standard from the Animal Ethics Committee at China Agricultural University, Beijing, China (AW32704202-2-15). Mice were selected as models in animal experiments. The random assignment was conducted under conditions where there was minimal variation in the health status of all samples/organisms. The protocols of all the animal experiments were permitted and carried out as requested. After anesthetized with 3% sodium pentobarbital, a hole around 1 cm in diameter on the epidermis was created. Then 200 μL of MRSA suspension (1×10^8 CFU/mL) was dropped onto the wound and incubated for 1 day. After that, 100 μL of liquid containing samples (SA/B-Uio-66 (Ce), B-Uio-66 (Ce), Uio-66 (Ce), and SA) was added to treat the infected wound. Normal saline, amoxicillin (10 μg/mL), and vancomycin (10 μg/mL) were also used as contrasts. After 12 days, the treated wounds were cut off and fixed with 10% formaldehyde solution for H&E stain, Masson trichrome, CD31, TNF-α, IL-4, IL-6, IL-13 immunohistochemistry, and iNOS/CD206 immunofluorescence analysis.

Statistical analysis

All experiments were performed as biological replicates at least three times. All data were expressed as mean values ± standard derivation (SD). All the quantitative data in each experiment were evaluated and analyzed using one-way ANOVA and Tukey–Kramer multiple comparisons test for multiple-group analysis in GraphPad Prism 8.0.2 software to evaluate the statistical significance of the variance. The p-value was used as a statistical significance threshold ($^{*}P < 0.05$, $^{**}P < 0.01$, $^{***}P < 0.001$, $^{****}P < 0.0001$).

Results and discussion

Synthesis and characterization of SA/B-Uio-66 (Ce)

In a typical synthesis procedure, multi-enzyme activity biocatalyst was synthesized via a one-pot solvothermal coprecipitation method using ammonium cerium (IV) nitrate as the metal ion source and 1,4-dicarboxybenzene (PTA) as the organic linker. Accompanied by subsequent modification and activation process to obtain 4-APBA modified and SA loaded Cerium-base MOF particles

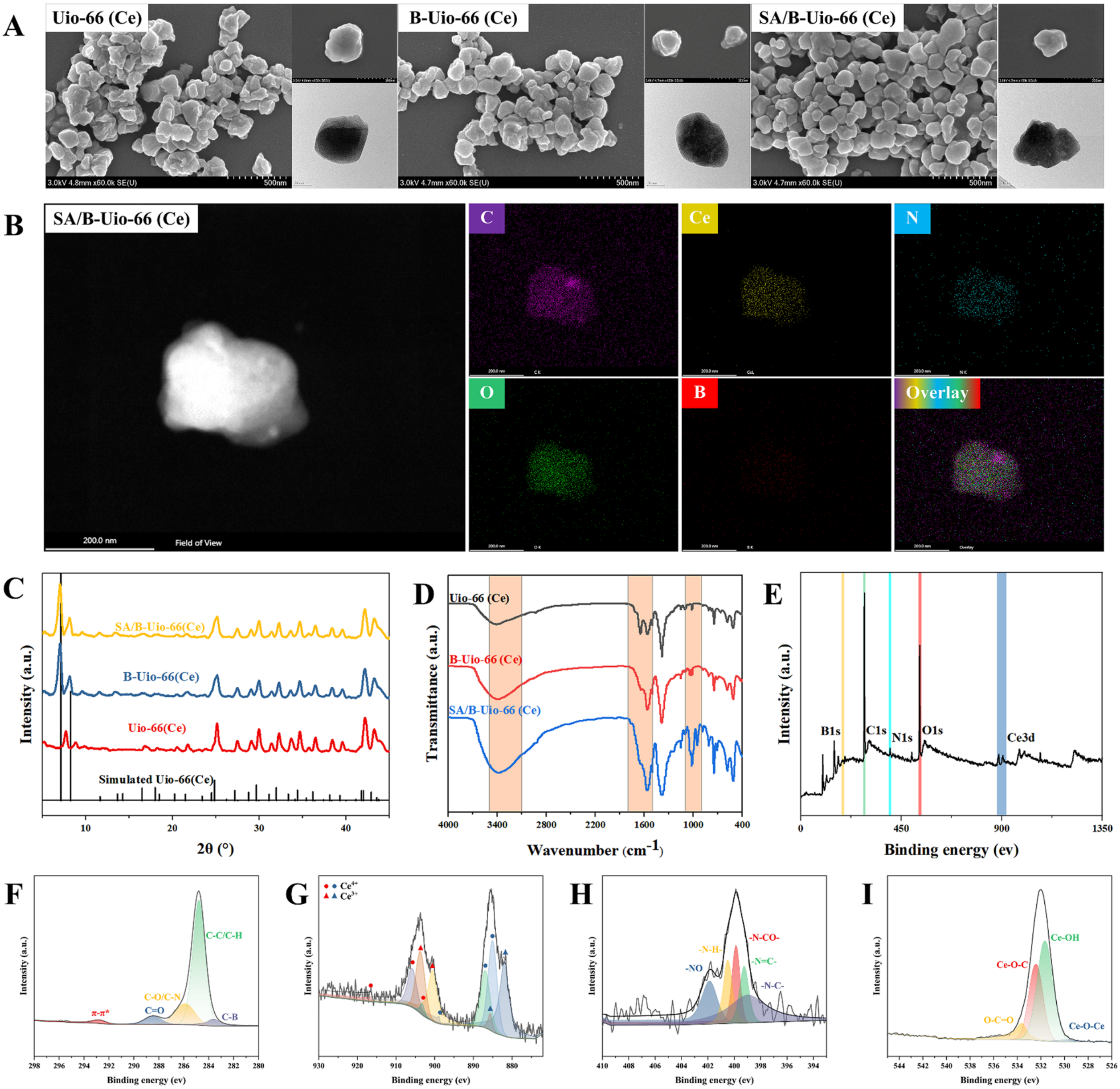

Fig. 1 Characterization. **A** SEM and TEM images of Uio-66 (Ce), B-Uio-66 (Ce), SA/B-Uio-66 (Ce). **B** Elemental mapping of SA/B-Uio-66 (Ce). **C** XRD patterns and **D** FTIR Spectrum of Uio-66 (Ce), B-Uio-66 (Ce) and SA/B-Uio-66 (Ce). **E** Full XPS spectrum XPS spectra of SA/B-Uio-66 (Ce). **F**–**I** XPS spectrum of C, Ce, N and O element, respectively

[named SA/B-Uio-66 (Ce)] to serve as controlled ROS regulation and MRSA targeting system. Scanning electron microscopy (SEM) and transmission electron microscopy (TEM) spectra reveal that B-Uio-66 (Ce) and SA/B-Uio-66 (Ce) adopt a typical Uio-66 (Ce) morphology with a similar average size of 198.13 ± 11.16 nm (Fig. 1A). In addition, the energy disperse spectroscopy (EDS) image illustrated the presence of Ce, O, N, B, and C, nearly uniformly distributed throughout the material, suggesting that the nanozymes are successfully and evenly modified with BA and SA (Fig. 1B and Fig. S1A). The quantitative atomic percentage results with N element to B element ratios greater than 1:1, indicating the presence of SA on the surface (Fig. S1B). The structure of SA/B-Uio-66 (Ce) was confirmed by X-ray diffraction (XRD) analysis, which showed characteristic peaks at 2θ values of 7.1°, 8.2°, 11.6°, 13.6°, and 14.3° corresponding to the (111), (200), (220), (311), and (222) planes, respectively (Fig. 1D).

Based on the results obtained from Fourier Transform Infrared (FTIR) spectroscopy (Fig. 1D), we conducted a detailed analysis of the characteristic vibrational modes of the materials investigated. The Uio-66 (Ce) framework (black spectrum) displays a prominent O–H stretching vibration peak at approximately 3400 cm^{-1}, signifying a substantial presence of hydroxyl groups, consistent with the structure of MOF. Additionally, C=O stretching vibrations observed near 1650 cm^{-1} and benzene ring vibrations around 1500 cm^{-1} indicate the successful incorporation of PTA. Upon modification with 4-APBA, represented by B-Uio-66 (Ce) (red spectrum), significant alterations in the vibrational peaks are evident. The changes observed around 3400 cm^{-1} and 1650 cm^{-1} suggest the introduction of N–H and O–H functionalities, reflecting interactions between the amino groups of 4-APBA and the surface carboxyl groups of Uio-66 (Ce). Furthermore, the emergence of benzene ring vibrations near 1500 cm^{-1} further substantiates the successful incorporation of the modifying agent. The SA/B-Uio-66 (Ce) composite (blue spectrum) reveals additional modifications in the vibrational patterns following the adsorption of SA. The peaks around 3400 cm^{-1} and 1650 cm^{-1} exhibit further shifts, indicating the influence of SA on the vibrational modes. Notably, the enhancement of the C-B stretching vibration around 1100 cm^{-1} suggests a strong interaction between SA and the modified framework.

To further confirm the chemical states of the elements in SA/B-Uio-66 (Ce) and the successful modification with 4-APBA and the loading with SA on the surface, we conducted X-ray photoelectron spectroscopy (XPS) and Zeta potential analysis (Fig. 1E–I and Fig. S1D). As illustrated in Fig. 1E, the full XPS spectrum of SA/B-Uio-66 (Ce) reveals distinct peaks for B 1 s (190.8 eV), C 1 s (284.8 eV), N 1 s (399.9 eV), O 1 s (532.0 eV), and Ce 3d (885.42 eV). These results indicate the successful modification of Uio-66 (Ce) with 4-APBA and the effective loading of SA on the surface, which was also proved by the zeta potential changes (Fig. S1D). The high-resolution C 1 s spectrum of SA/B-Uio-66 (Ce) exhibited five distinct peaks (Fig. 1F), assigned to various carbon species associated with 4-APBA, SA, and the PTA ligand. The characteristic peaks at 283.6 eV for C-B and 285.8 eV for C-O/C-N indicate the modification by 4-APBA and the loading of SA, respectively [48, 49]. Additionally, the peak at 292.8 eV features an overlapping π–π* shake-up satellite, attributed to sp^2 aromatic carbon from the PTA ligands [50]. The Ce 3d XPS spectrum of SA/B-Uio-66 (Ce) revealed the presence of Ce ions in multiple valence states (Fig. 1G), displaying six peaks corresponding to the spin–orbit splitting of Ce (IV) 3d5/2 (red circle) and 3d3/2 (blue circle) orbitals, as well as four peaks associated with Ce (III) 3d5/2 (red triangle) and 3d3/2 (blue triangle) orbitals. The binding energies for Ce (IV) 3d3/2 and 3d5/2 were found to be 917.0, 907.2, and 901.7 eV (red circle) and 898.5, 887.1, and 885.1 eV (blue circle), respectively. The binding energies for Ce (III) 3d3/2 and 3d5/2 were 904.0 and 900.3 eV (red triangle) and 887.3 and 881.4 eV (blue triangle), respectively. The surface ratio of Ce(III) was calculated to be approximately 50.25% (Table S1), suggesting that each $Ce_6O_4(OH)_4$ cluster on the surface contains an average of three Ce (III) and three Ce (IV) ions. The N 1 s spectrum of SA/B-Uio-66 (Ce) displayed five distinct peaks (Fig. 1H), associated with various nitrogen species on the surface. The peak at 399.3 eV corresponds to pyridine nitrogen, indicative of SA loading, while the peak at 399.9 eV is linked to the amide nitrogen group, confirming the surface modification by 4-APBA via the EDC/NHS reaction. The O 1 s spectrum revealed four distinct peaks (Fig. 1I), assigned to different oxygen species within the Ce_6 cluster and the PTA ligand: uncoordinated carboxyl groups of the PTA ligands (O–C=O, 533.5 eV), coordinated carboxylate between the PTA and Ce_6 cluster (Ce–O–C, 532.5 eV), unsaturated cerium hydroxyl active sites (Ce–OH, 531.6 eV), and bridging oxide bonds within Ce_6 clusters (Ce–O–Ce, 529.8 eV). Notably, the peak attributed to unsaturated Ce–OH (531.6 eV) constituted a relatively high proportion (50.4%) among the four O 1 s peaks (Table S2), indicating an abundance of Ce-OH active sites on the surface [36]. The thermal stability of the substance was evaluated using TGA, which measures weight loss as a function of temperature changes. The TGA curves (Fig. S1E) reveal three distinct thermal degradation stages occurring between 25 °C and 900 °C for the nanozymes. The first stage, occurring from 50 °C to 300 °C, is attributed to the loss of free and bound water from Uio-66 (Ce), resulting in a mass reduction of approximately 16%. In the case of B-Uio-66 (Ce) and SA/B-Uio-66 (Ce), this initial weight loss extends up to around 480 °C, with mass reductions of 33% and 28%, respectively. This suggests that, in addition to the loss of free and bound water, there may also be thermolysis of surface-modified structures. The second stage, characterized by rapid weight loss occurring between 500 °C and 620 °C, signifies the oxidation and decomposition of carbonaceous materials under heat. Notably, SA/B-Uio-66 (Ce) demonstrates a relatively lower and broader thermal decomposition temperature range. The derivative thermogravimetric curve (Fig. S1F) indicates that the decomposition peaks for B-Uio-66 (Ce) and SA/B-Uio-66 (Ce) shift towards higher temperatures, suggesting that modifications to the surface structure enhance the stability of the material's carbonization under elevated thermal conditions.

Multienzyme activity and chemodynamic assessments

CDT is widely recognized for its potent bactericidal ability, effectively addressing the challenges posed by antibiotic resistance through the generation and action of ROS [51, 52]. Therefore, it is essential to investigate the ROS-producing potential of the composite materials. To systematically evaluate the multienzyme catalytic activity

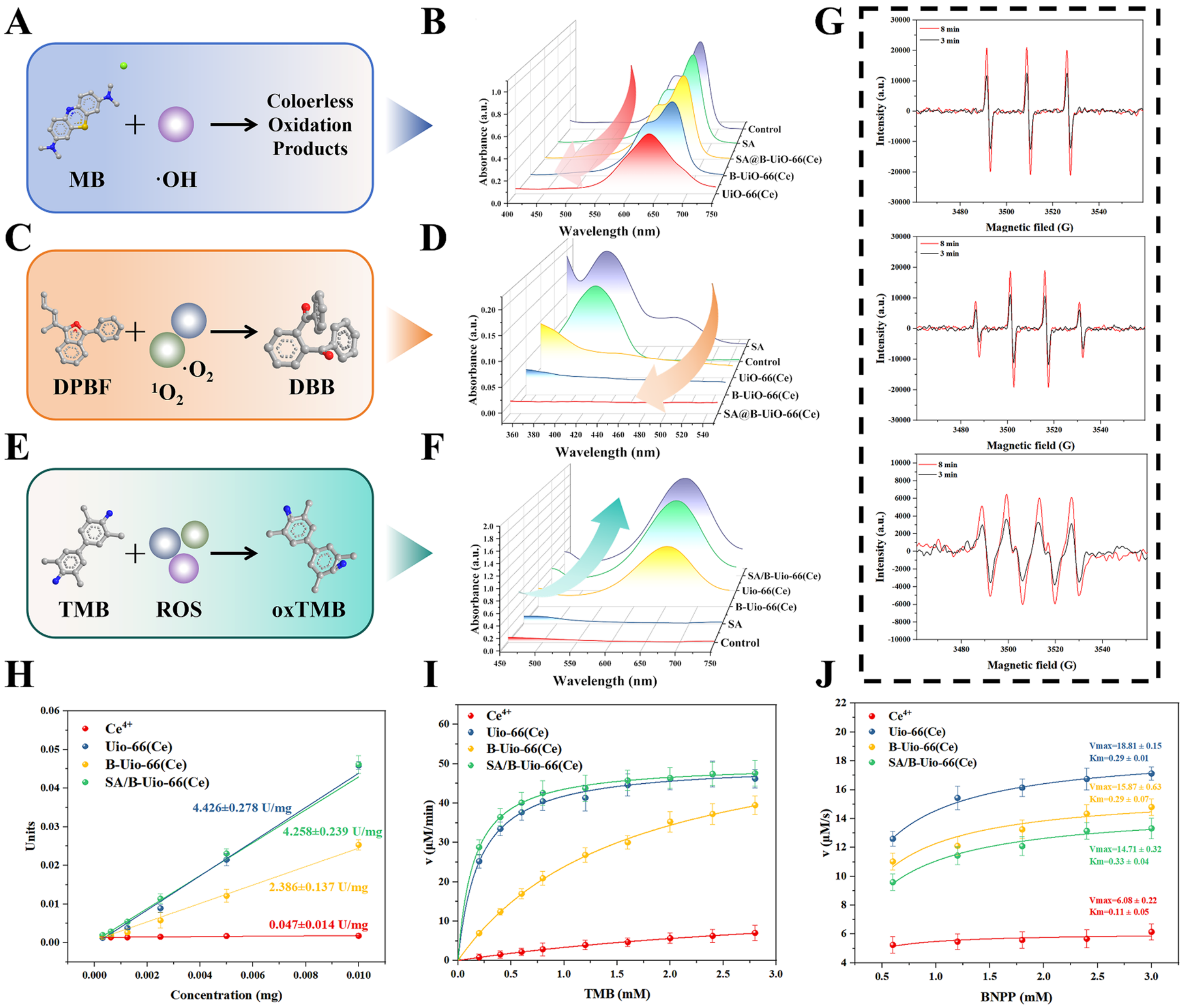

Fig. 2 Multienzyme activity performance of nanocatalytic system. **A** Chemical reaction diagram of MB oxidation. **B** MB consumptions of different nanozymes. **C** Chemical reaction diagram of DPBF oxidation. **D** DPBF consumptions of different nanozymes. **E** Chemical reaction diagram of TMB oxidation. **F** TMB consumptions of different nanozymes. **G** ESR spectra of ·OH, 1O2 and $·O_2^-$. **H** Specific activities of oxidase in different nanozymes. Michaelis–Menten curves of **I** oxide enzyme and **J** phosphatase activities for different nanozymes

of the complex, we first examined its oxidase activity in a hydrogen peroxide-free environment. MB, a dye extensively used in scientific research and various applications, demonstrates exceptional sensitivity to ·OH, making it an ideal candidate for detecting their presence (Fig. 2A). As shown in Fig. 2B, the SA/B-Uio-66 (Ce) group exhibited significantly lower absorbance intensity compared to the control groups, indicating successful generation of ·OH. However, the yield was slightly lower compared to Uio-66 (Ce) and B-Uio-66 (Ce), likely due to partial shielding of the catalytic sites caused by surface modification and adsorption.

Similarly, Fig. 2D illustrates the continuous fluorescence degradation of DPBF by a series of nanozymes, attributed to the generation of $^1O_2$. TMB, a typical substrate used in colorimetric assays, shows remarkable sensitivity to ROS (Fig. 2E), further underscoring its applicability for detection. As depicted in Fig. 2F, the SA/B-Uio-66 (Ce) group exhibited significantly higher absorbance intensity than the other groups, indicating its capability to generate ROS. Following the methodology established by Yan et al., we systematically assessed the enzyme activity kinetics of various biocatalysts using specific activity, K_m, and V_{max} as quantitative metrics (Fig. 2H, I) [47]. The oxidase activity of SA/B-Uio-66 (Ce) constructed in this study outperforms several reported nanozymes in the literature (Table S3).

To further investigate the types of ROS produced by SA/B-Uio-66 (Ce), electron spin resonance (ESR) signals were collected using the spin traps 5,5-dimethyl-1-pyrroline N-oxide (DMPO) and 2,2,6,6-tetramethylpiperidine-1-oxyl (TEMP). As illustrated in Fig. 2G, three distinct TEMP $^1O_2$ peaks were observed with a height ratio of 1:1:1, indicating the generation of $^1O_2$. Additionally, four distinct DMPO-·OH peaks with a height ratio of 1:2:2:1 confirmed the production of ·OH. The presence of $O_2^{\cdot -}$ was also identified, with signal peaks exhibiting a height ratio of 1:1:1:1. The catalase (CAT) activity of SA/B-Uio-66 (Ce) was validated using 3-carbamoyl-2,2,5,5-tetramethyl-3-pyrroline-1-yloxyl (CTPO) as an O_2-sensitive spin-label probe (Fig. S2), corroborating the findings of Shan et al. [36].

Furthermore, we measured the phosphatase-like activity of various cerium-based biocatalysts by employing different concentrations of bis(4-nitrophenyl) phosphate (BNPP) as a model substrate, quantifying the results in terms of K_m and V_{max}. As shown in Fig. 2J, these findings indicate that SA/B-Uio-66 (Ce) has the potential to disrupt bacterial phosphate esters, encompassing the degradation of extracellular and intracellular DNA as well as interference with nucleic acid and energy metabolism critical for bacterial survival during biofilm infections. Furthermore, these findings not only confirm the successful surface modification of the bare MOF but also indicate that such modifications may partially reduce the affinity of nanzyme materials for phosphate-ester substrates, thereby influencing their catalytic activity [53].

Additionally, the peroxidase-like activity of the series of materials was evaluated using the aforementioned methods (Fig. S3A, B). By controlling the presence or absence of hydrogen peroxide and oxygen in the reaction system, we demonstrated that the material can generate hydroxyl radicals using dissolved oxygen, water molecules, and hydrogen peroxide as substrates, with yields correlating with substrate type and abundance (Fig. S3C-F). Collectively, these results confirm that SA/B-Uio-66 (Ce) can controll the modulation of ROS in the microenvironment of antibiotic-resistant bacterial infections, thereby exerting its antimicrobial effects.

As previously noted, the SA/B-Uio-66 (Ce) exhibited superior catalytic performance compared to Uio-66 (Ce) and B-Uio-66 (Ce). To further elucidate the potential mechanisms underlying the rapid reaction kinetics at the cerium sites in this biomimetic catalytic delivery system, we employed UV–vis-NIR diffuse reflectance spectra, micro-area XPS, and Brunauer–Emmett–Teller (BET) surface area analysis. The results (Fig S4 and S5) demonstrated that the direct bandgap of Uio-66 (Ce) decreased significantly upon surface modification with 4-APBA, and further adsorption of SA led to an additional reduction in the direct bandgap. Concurrently, the valence bands of all three nanomaterials also exhibited a decline due to surface modifications. These reductions in both the direct bandgap and the valence band indicate a decrease in the energy required for electron transitions between the valence and conduction bands, thereby enhancing the efficiency of charge carrier generation and improving catalytic activity. However, enzymatic kinetics revealed that the catalytic efficiency of B-Uio-66 (Ce) was lower than that of the other two catalysts, suggesting that, in addition to the electronic band structure, other factors also influence the catalytic performance of the delivery system. Analysis of the surface area and pore size for the MOF nanozymes (Fig. S5) showed that the degree of pore accessibility and specific surface area for B-Uio-66 (Ce) and SA/B-Uio-66 (Ce) were both reduced compared to Uio-66 (Ce). This indicates that the modification with 4-APBA not only improved surface characteristics but also obscured the catalytic cerium sites. Notably, after treatment with SA, the pore accessibility and specific surface area of SA/B-Uio-66 (Ce) increased relative to B-Uio-66 (Ce), suggesting that adsorption of SA may facilitate the reopening of previously shielded sites while potentially reducing surface charge. In summary, SA/B-Uio-66 (Ce) demonstrates enhanced catalytic performance compared to both Uio-66 (Ce) and B-Uio-66 (Ce).

Antibacterial activity test in vitro

Inspired by the remarkable properties of these nanozymes, including controlled ROS regulation and phosphate-ester hydrolysis, we investigated the synergistic antibacterial efficacy of B-Uio-66 (Ce) and SA to enhance the capture of drug-resistant planktonic bacteria, specifically using MRSA as our model organism. Initially, we systematically assessed the cytotoxicity and synergistic antibacterial effect of the catalyst system in conjunction with SA through fractional inhibitory concentration (FIC) experiments (Fig. S6; Fig. S7). Notably, even at a low concentration of SA (0.625 μg/mL), cell viability remained below 70%. However, the addition of B-Uio-66 (Ce) significantly restored cell viability, indicating that B-Uio-66 (Ce) can mitigate the cytotoxicity of SA and enhance its biocompatibility. Furthermore, surviving bacterial counts post-treatment were evaluated using the dilution plate method. The results demonstrate that the incorporation of B-Uio-66 (Ce) significantly enhances antibacterial activity, even at low concentrations of SA. This finding provides valuable theoretical support for the development of a safe composite drug delivery platform that integrates CDT materials with natural antibacterial components, aiming to reduce toxicity while improving the efficacy of natural antibacterial agents.

As illustrated in Fig. 3A, B, we quantified bacterial content following incubation with various materials under different conditions. The group treated with B-Uio-66 (Ce) exhibited a significantly lower bacterial survival rate compared to the bare Uio-66 (Ce), even at low concentrations. This finding suggests that surface-targeting ligand modifications of the nanozymes enhance their enrichment and promote the accumulation of ROS around the bacteria, thereby improving antibacterial efficacy, a conclusion further supported by SEM visualizations (Fig. 3C). Moreover, the SA/B-Uio-66 (Ce) formulation, treated at the same concentration, demonstrated superior antibacterial effectiveness compared to other nanozyme treatment groups. SEM/TEM/EDS images confirmed that the SA/B-Uio-66 (Ce) effectively localized and captured MRSA, with visible distortions and morphological collapse indicating irreversible destruction (Fig. 3D, S8A). To further validate the targeting of MRSA, CLSM visualization (Fig. S8b) of MRSA treated with rhodamine B-labeled B-Uio-66 (Ce) showed that the presence of green fluorescent clusters closely aligned with the distribution of red fluorescent dots along the surface and edges of the particles, resulting in overlapping areas that exhibited yellow fluorescence. Nearly all green fluorescently labeled bacteria displayed a dense coating of red fluorescent material. A similar phenomenon was observed in the rhodamine B-labeled Uio-66 (Ce) treatment group; however, the number and intensity of red and yellow fluorescently labeled bacteria was comparatively lower..The bacterial growth curve further validated the sustained inhibition of drug-resistant bacterial growth by our composites (Fig. 3E). Additionally, a LIVE/DEAD fluorescence assay was conducted to visualize the distribution of viable and non-viable planktonic MRSA (Fig. 3F). Notably, the SA/B-Uio-66 (Ce) group exhibited a higher and more persistent red fluorescence compared to other treatment groups. The corresponding quantitative results presented in Fig. 3G indicate that the majority of bacteria in the SA/B-Uio-66 (Ce) group were killed, underscoring its significant potential against MRSA, which is confirmed with spread plate counting and SEM/TEM observations.

What is worse, in addition to their planktonic forms, MRSA exhibits a propensity to self-organize into structured, resilient biofilms, which impede the efficacy of antimicrobial interventions [54]. Bacterial populations embedded within these biofilms display increased resistance to antimicrobial treatments, leading to persistent infections and significant hindrances in wound healing [55]. Consequently, the capacity of SA/B-Uio-66 (Ce) to disrupt mature biofilms is crucial for promoting wound healing. To evaluate this, pre-formed biofilms were treated with PBS (control), Uio-66 (Ce), B-Uio-66 (Ce), SA, or SA/B-Uio-66 (Ce), and biofilm disruption was assessed using crystal violet staining. As illustrated in Fig. 4A, the intensity of purple coloration in the cerium-based nanozyme groups significantly diminished compared to the SA treatment. The disruption rates of the biofilms, presented in Fig. 4B, indicate that SA/B-Uio-66 (Ce) effectively disrupts biofilms due to its synergistic combination of multi-enzyme-like properties and natural antimicrobial activity. Importantly, inhibiting biofilm maturation emerges as a valuable strategy for enhancing wound healing. MRSA was co-incubated with various treatments to form biofilms, which were subsequently stained with crystal violet. Remarkably, this biofilm inhibition strategy resulted in substantial biofilm removal, with the coloration in the SA/B-Uio-66 (Ce) group nearly disappearing post-treatment. The rate of biofilm inhibition corresponded with the antibacterial activity's intensity across the different treatment groups, with SA/B-Uio-66 (Ce) demonstrating the most pronounced effect on inhibiting biofilm maturation (Fig. 4C). This outcome may be attributed to the direct bactericidal effects of the treatments on planktic bacteria during the early stages of biofilm formation, thereby reducing the viable bacterial count and influencing the biofilm development process. Additionally, three-dimensional fluorescence images obtained via laser confocal microscopy provided clear visualization of the extent of biofilm disruption and inhibition (Fig. 4D). Quantitative analysis

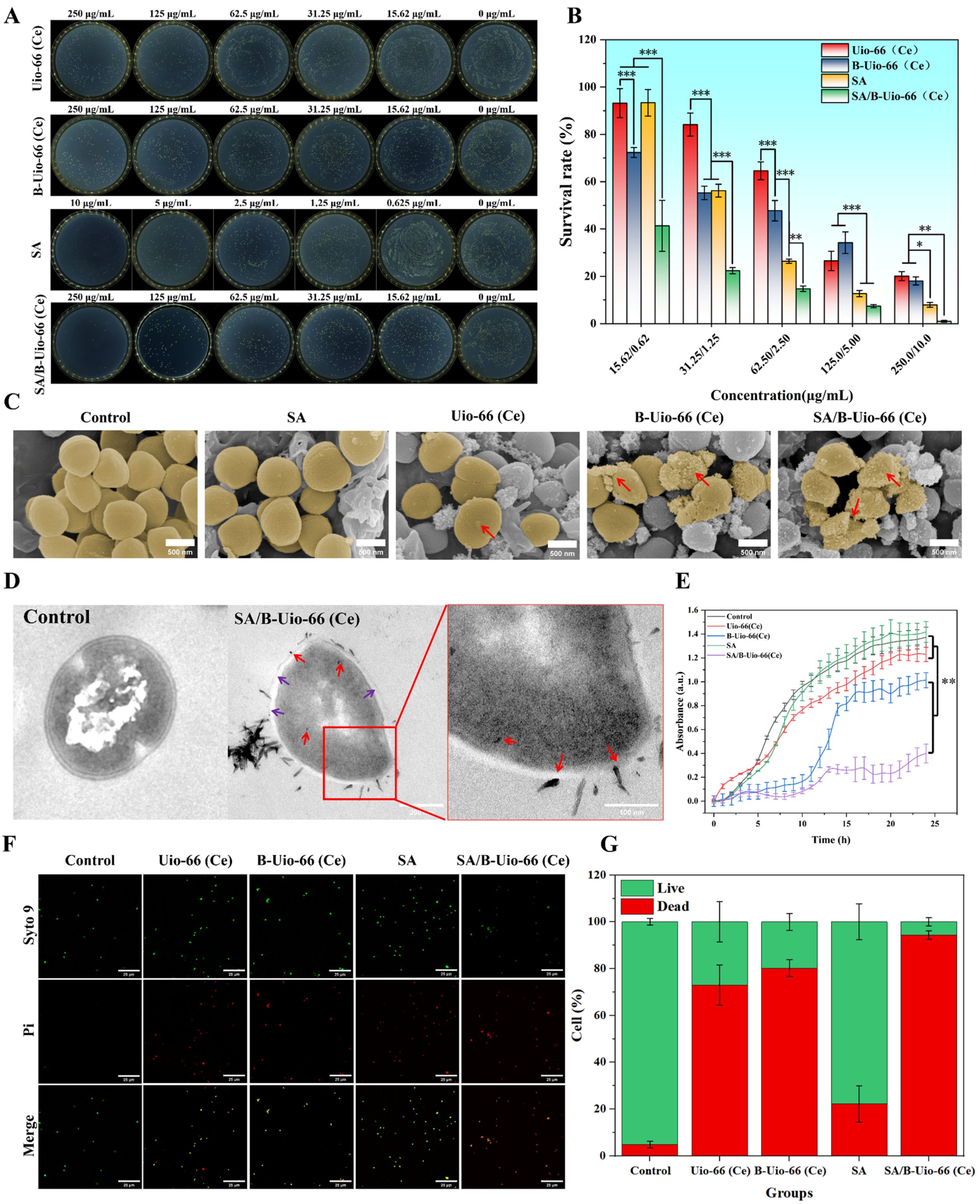

Fig. 3 In vitro antibacterial performance of different nanozymes. **A** Photographs of bacterial colonies and **B** relative bacterial viability of MRSA under different conditions. **C** Typical SEM and **D** TEM images of MRSA after various treatments. **E** The growth curve of bacteria after various treatments. **F** Fluorescence images and **G** quantitative analysis of dead (red) and live (green) bacteria of MRSA in different treatment groups. (Data are presented as mean ± SD. Significance between two groups was calculated using one-way ANOVA and Tukey–Kramer multiple comparisons test. n = 3. ***p < 0.001, **p < 0.01 and *p < 0.05 same below)

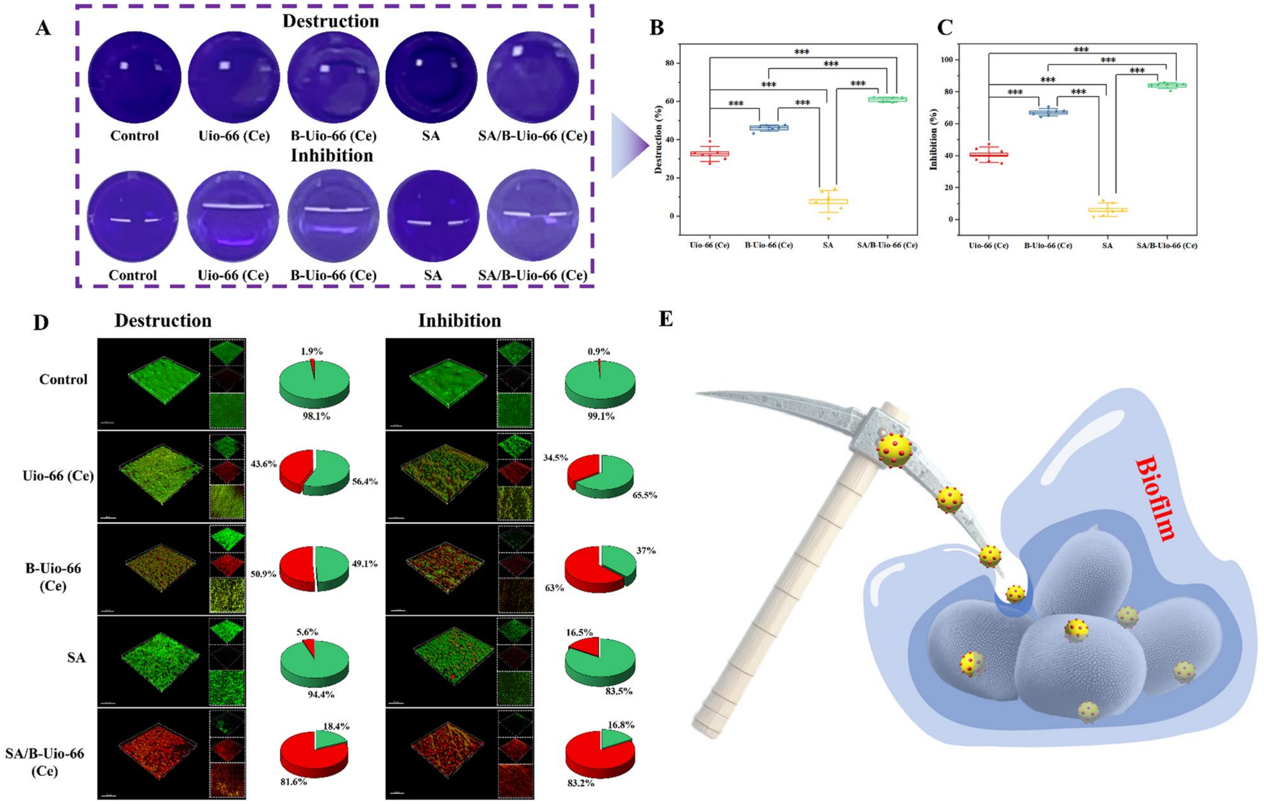

Fig. 4 Anti-biofilm ability of nanocatalytic system in vitro. **A** Representative MRSA biofilms stained with crystal violet dye following various treatments. The associated quantitative analysis for biofilms **B** destruction and **C** inhibition. **D** Reconstructed 3D images of the treated biofilms through LIVE/DEAD staining. **E** In vitro bacteria killing procedure illustrated schematically

of MRSA destruction and inhibition through fluorescence intensity corroborated these findings. Additionally, we investigated the effects of varying concentrations of SA/B-Uio-66 (Ce) (62.5, 125, and 250 μg/mL) and different exposure times (6, 12, 24, and 36 h) on biofilm disruption. The results from crystal violet staining indicated a positive correlation between the biofilm disruption rate and both the concentration and incubation duration (Fig. S8 D, E). Specifically, higher concentrations and longer exposure times led to more effective penetration and destruction of the biofilm. These findings suggest that concentration and retention time are crucial factors influencing the efficacy of biofilm removal. While SA alone can partially clear biofilms, the free drug often suffers from insufficient retention time, which diminishes its penetration ability. In contrast, nanoparticles formed by loading SA onto B-Uio-66 (Ce) significantly enhance retention time, and the inherent phosphatase activity of B-Uio-66 (Ce) further improves its penetration and biofilm disruption capabilities. Lin et al. demonstrated that encapsulating magnolol in nanomicelles enhanced its penetration and eradication effects against *Staphylococcus aureus* biofilms [56]. Moreover, our study revealed that B-Uio-66 (Ce) exhibited greater biofilm disruption capabilities compared to Uio-66 (Ce) at the same concentration. This enhanced efficacy may be attributed to the boronic acid surface modification, which can bind not only to the cis-diol groups on the bacterial surface but also to the cis-diol groups of polysaccharides in the extracellular matrix of the biofilm. This interaction likely increases both retention time and local concentration, thereby enhancing the effectiveness of biofilm removal. These results indicate that the SA/B-Uio-66 (Ce) combination not only disrupts and inhibits biofilm formation but also enhances bacterial eradication (Fig. 4E), thereby facilitating wound healing. In conclusion, the composite platform SA/B-Uio-66 (Ce), characterized by its multi-enzyme activity and ability to target drug-resistant bacteria while augmenting chemotherapeutic effects, exhibits significant potential for inhibiting biofilm formation and eradicating mature biofilms, ultimately promoting the healing of infected skin wounds.

These results collectively indicate that the multifaceted antibacterial system, composed of natural antimicrobial agents and biocatalysts with multi-enzyme activity, effectively addresses the limitations of single-mechanism approaches, which often exhibit poor antibacterial performance and insufficient biofilm penetration and clearance. Additionally, this system offers a promising solution for the challenges associated with the high toxicity of natural antimicrobial chemotherapy agents, facilitating the development of safer alternatives.

Antimicrobial mechanism of SA/B-Uio-66 (Ce)

The bacterial membrane potential, defined as the potential difference between the internal and external environments of bacteria, is a crucial factor for sustaining bacterial life. To investigate the biological properties of bacterial membranes following ROS disruption, we employed a fluorescent probe, 3,3-dipropylsulfur dicarbocyanine iodide ($DiSC_3(5)$), to assess changes in the membrane potential of MRSA under various treatments. A decrease in membrane potential leads to the aggregation of $DiSC_3(5)$, resulting in an increased fluorescence signal as the potential diminishes. As illustrated in Fig. S9A, C, the control group exhibited no green fluorescence, while all nanozyme treatment groups displayed significant green fluorescence, particularly the SA/B-Uio-66 (Ce) group, indicating a marked reduction in membrane potential. These results reflect the extent of bacterial membrane disruption across different treatments. Additionally, ROS generation during the antibacterial process was validated using 2′,7′-dichlorofluorescein diacetate (DCFH-DA). As shown in Fig. S9B, the control group exhibited no fluorescence, suggesting low levels of intracellular ROS production. In contrast, green fluorescence signals were detected in all nanozyme treatment groups, demonstrating the chemodynamic capabilities of the bare MOF and its inherent antibacterial potential. Notably, fluorescence emission was most pronounced in the SA/B-Uio-66 (Ce) group, indicating that targeted modification and SA loading enhance bacterial oxidative stress. The quantification results of DCFH-DA fluorescence are presented in Fig. S9D. The results indicate that the ROS generated by SA/B-Uio-66 (Ce) effectively disrupt the bacterial cell membrane, leading to the disturbance of membrane surface potential and hindering electron transfer, which ultimately triggers oxidative stress responses within the bacteria.

To elucidate the impact of ROS and multi-enzyme activity on bacterial metabolic processes, we initially examined the direct interactions of all treatments with ATP. As shown in Fig. S9E, all cerium-based nanozymes significantly reduced ATP levels, with the 4-APBA-modified nanozyme exhibiting the most pronounced effect. This reduction may result from the direct binding of nanozymes to ATP, leading to the cleavage of phosphodiester bonds. Additionally, the surface modification with phenylboronic acid decreases the physical distance between the enzyme and its catalytic substrate by forming reversible covalent bonds with ribose in ATP, thereby enhancing ATP degradation. To further validate the efficacy of the nanocatalytic system on the energy metabolism of MRSA, we quantitatively analyzed intracellular ATP levels in each treatment group (Fig. S9F). Interestingly, different from the results of direct interaction tests, the SA treatment group demonstrated a significant reduction in intracellular ATP levels. This decrease is primarily attributed to SA functioning as a natural antibacterial small molecule that inhibits ATP production by modulating the energy metabolism pathways of MRSA. Furthermore, the nanozyme treatment also lowered total ATP content within the bacterial cells, particularly in the SA/B-Uio-66 (Ce) group. This finding suggests that the bacteria enter a necrotic or toxic state following treatment with SA/B-Uio-66 (Ce), and that SA/B-Uio-66 (Ce) effectively integrates phosphodiesterase activity with the metabolic regulatory functions of SA.

In addition to their impact on energy metabolism, cerium-based catalytic materials have demonstrated phosphatase-like hydrolytic activity. Consequently, we scrutinize the integrity of nucleic acid (DNA and RNA) after each treatment regimen. We further investigated their effects on nucleic acids. A 2000 bp DNA fragment was extracted from MRSA and treated with various groups, with the relative quantification data presented in Fig. S9G. Notably, treatment with the nanomaterials resulted in a reduction of total DNA content. Moreover, compared to the control group, the level of DNA fragmentation was significantly increased following treatment with SA/B-Uio-66 (Ce) (Fig. S6J, M). Additionally, total intact bacterial DNA was extracted from the different treatment groups, and analyzed the corresponding quantitative data (Fig. S6H, I). Remarkably, only a minimal amount of intact DNA was detected in the SA/B-Uio-66 (Ce) group. Concurrently, agarose gel electrophoresis revealed substantial degradation of genomic DNA in the SA/B-Uio-66 (Ce) treatment group (Fig. S6K, N). Similar results were observed in the same trials for extracted genomic RNA. This indicates that bacterial DNA/RNA undergoes severe damage due to the multienzyme activity by SA/B-Uio-66 (Ce).

In summary, SA/B-Uio-66 (Ce) exhibits significant antibacterial effects, primarily attributed to the synergistic action of its multi-enzyme activity and natural antibacterial agents. The antibacterial mechanism of SA/B-Uio-66 (Ce) is multifaceted. Upon contact with bacteria, SA/B-Uio-66 (Ce) induces membrane potential polarization, thereby increasing bacterial membrane permeability. This facilitates the internalization of catalytic substrates and SA into the bacterial cells. These antibacterial components exert their lethal effects through various mechanisms, including disruption of intracellular metabolism, inhibition of ATP activity, damage to DNA/RNA, and induction of oxidative stress. Ultimately, these processes lead to the complete elimination of the bacteria.

Transcriptome analysis of MRSA

To comprehensively investigate the antimicrobial mechanism of SA/B-Uio-66 (Ce), mRNA sequencing analysis was performed on MRSA. As illustrated in Fig. 5A, B, a total of 261 genes were found to be upregulated, while 290 genes exhibited downregulation in the SA/B-Uio-66 (Ce) treatment group compared to the control group. Additionally, the heatmap (Fig. 5C) highlights the metabolic differences between the two groups. Gene Ontology (GO) analysis revealed that these differentially expressed genes (DEGs) are primarily associated with various biological processes and molecular functions (Fig. S10). Notably, the enriched GO analysis indicates that biosynthetic processes are significantly impacted by SA/B-Uio-66 (Ce) treatment, particularly those involved in nucleotide biosynthesis and metabolism (e.g., purA, carA, and pyrC), cellular amino acid biosynthesis and metabolism (e.g., arcC, pyrB, and asd), as well as transmembrane transporter activity (e.g., brnQ, glcU, and narT) and ATPase activity (e.g., secA2 and secG). The genes associated with biosynthesis are implicated in MRSA virulence factors, lipid peroxidation, bacterial nutrient uptake, and metabolism. The terms related to transporter and ATPase activity represent the most affected molecular functions, suggesting compromised bacterial membrane integrity. The downregulation of these genes could significantly impair MRSA's ability to colonize and proliferate (Fig. S11A, B). Furthermore, bacterial growth is heavily reliant on protein synthesis, which is catalyzed by the ribosome, an abundant and highly complex structure whose assembly and function are crucial for bacterial physiology. The upregulation of ribosomal protein genes (e.g., rpsP, rpsD, and rplM) indicates an active state of protein synthesis within the bacteria. The discrepancy between inhibited transmembrane transport and the upregulated protein synthesis serves to exacerbate metabolic disturbances within the bacteria. Moreover, SA/B-Uio-66 (Ce) inhibits MRSA biofilm activity by obstructing bacterial adherence, including the synthesis of capsular polysaccharides (e.g., cap8D, cap8E, and cap8F). This suppression diminishes bacterial virulence and impacts biofilm survival by disrupting the aggregation and binding of EPS, thereby affecting the formation and maturation of biofilm. These DEGs suggest that the oxidative stress induced by SA/B-Uio-66 (Ce) triggers significant metabolic dysregulation and intracellular stress in the affected microbes.

Additionally, the results of the Kyoto Encyclopedia of Genes and Genomes (KEGG) pathway enrichment analysis indicate a significant impact on metabolism, particularly concerning amino acid biosynthesis and metabolism (including arginine, lysine, alanine, aspartate, glutamate, proline, glycine, serine, threonine, and tryptophan), nitrogen metabolism, and nucleoside metabolism (both purine and pyrimidine), among others (Fig. 5D and Fig. S12). These pathways are associated with biofilm formation and detachment and play crucial roles in proliferation, drug resistance, and pathogenicity [57, 58]. The differentially expressed genes (DEGs), both downregulated and upregulated, are also illustrated (Fig. S13A-D). The inhibition of ABC transporter protein genes (e.g., ugpC, opp3C, and opuCA), which regulate ATP hydrolysis and transport, significantly impacts the nutrient uptake mechanisms in MRSA [59]. Notably, several drug resistance-related pathways, including beta-lactam resistance, vancomycin resistance, and cationic antimicrobial peptide (CAMP) resistance, were downregulated. This suggests that SA/B-Uio-66 (Ce) may decelerate the development of MRSA resistance through a multifaceted antibacterial action involving multi-enzyme activity combined with natural antibacterial agents, potentially weakening existing resistance. Furthermore, the activation of oxidative phosphorylation indicates that the bacteria are under oxidative stress [60, 61]. The expression of genes related to energy metabolism showed significant downregulation following SA/B-Uio-66 (Ce) treatment (Fig. S14), affecting pathways such as the pentose phosphate pathway (e.g., hxlA), glycolysis/gluconeogenesis (e.g., gap, adhP, and acsA), and the citrate cycle (e.g., icd, odhA, and fumC). This downregulation suggests a compromised energy supply for the bacteria. Concurrently, genes involved in sugar biosynthesis (e.g., cap8D, glmU, and cap8G) and the two-component system (e.g., dltD, phoP, and arlS) were also downregulated, indicating that the treatment may disrupt the formation and maturation of MRSA biofilms, potentially reducing their pathogenicity and infectivity. It has been proved that SA can effectively eliminate MRSA by interfering with the permeability of the cell wall and membrane and inducing the production of bacterial ROS. Additionally, it can disrupt biofilms by interfering with amino acid and energy metabolism processes [62–64]. Other studies indicated ROS can effectively disrupt biofilms, bacterial membranes, nucleic acids, and proteins at infection sites, leading to bacterial inactivation [65]. Compared to traditional antibiotics, ROS-based antibacterial strategies utilizing nanozymes significantly reduce the risk of developing resistance [14]. In summary, SA/B-Uio-66 (Ce), the Multi-enzymatic biomimetic antibacterial platform, integrates the antibacterial effects of ROS and SA. The ROS disrupts the integrity

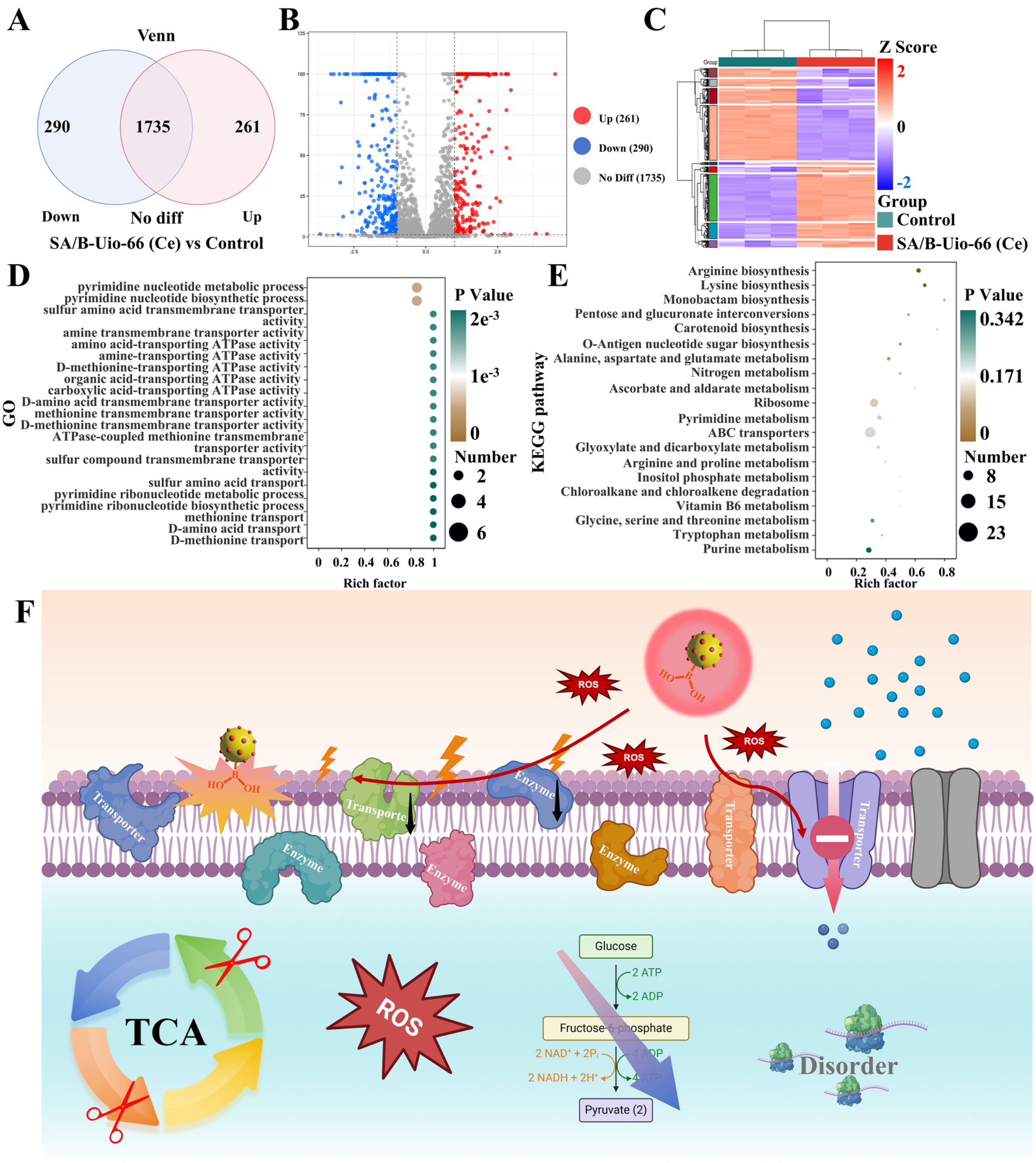

Fig. 5 Transcriptome analysis of MRSA with SA/B-Uio-66 (Ce) treatment. **A** DEG Venn diagram and **B** volcano plot. The blue and rose red dots indicate DEGs that are downregulated and upregulated, accordingly. **C** The heatmap numbers show the levels of comparative expression (red represents genes with relatively high expression levels, blue represents genes with relatively low expression levels). **D** GO enrichment evaluations of all DEGs. **E** KEGG enrichment analysis of all DEGs. **F** Schematic diagram of the mechanism by which SA/B-Uio-66 (Ce) affects biosynthesis and the preservation of MRSA in vitro

and permeability of bacterial cell walls and membranes, facilitating the delivery of SA into bacterial cells. Inside the bacteria, oxidative stress is further induced, resulting in lipid peroxidation and oxidative phosphorylation, which ultimately damage DNA and proteins. This disruption affects nucleotide and amino acid transport channels and interferes with genes related to biosynthesis and maintaining the bacterial intracellular and extracellular environment. Additionally, the expression of resistance genes is downregulated, while the inhibition and eradication of biofilms are enhanced (Fig. 5F). Together, these mechanisms realize the synergistic antibacterial effects of chemical kinetic therapy and SA.

Biocompatibility evaluation

The potential cytotoxicity of biomaterials has long been a concern in biomedicine, prompting extensive investigations [66–68]. Prior to conducting animal experiments, we assessed the biosafety of SA/B-Uio-66 (Ce) using the mouse fibroblast cell line (L929), in addition to the previously mentioned study on the combined cytotoxicity of SA and B-Uio-66 (Fig. S7). Cytocompatibility assessments were conducted using the cell counting kit (CCK-8) and hemolysis tests, as illustrated in Fig. 6A, B, and Fig. S15. The cytotoxicity and hemolysis of B-Uio-66 (Ce) were found to be lower than those of bare Uio-66, which may be attributed to charge reversal effects that reduce damage to the cell membrane due to 4-APBA modification. SA exhibited significant cytotoxicity against L929 cells at a low concentration of 1.25 μg/mL. Notably, hemolysis induced by SA occurred only at a high concentration of 10 μg/mL. This discrepancy may be related to the differing sensitivities of various cell types to SA. Importantly, for SA/B-Uio-66 (Ce), cell proliferation rates remained above 80%, and hemolysis rates were below 5% compared to the control group, even at a high concentration of 250 μg/mL after incubation. Additionally, L929 cells treated with SA/B-Uio-66 (Ce) were stained with Calcein/PI for visualization of cell mortality, revealing less red fluorescence in the treatment group (Fig. 6C). These results indicate excellent cytocompatibility of SA/B-Uio-66 (Ce). To further evaluate the biosafety of SA/B-Uio-66 (Ce) in vivo, mice were treated intraperitoneally with various antibacterial systems. Histological examination using H&E staining of major organs (heart, liver, spleen, lung, and kidney) (Fig. 6D), along with blood routine and biochemical tests, revealed no significant changes compared to the control group (Fig. S16). Collectively, the in vivo and in vitro results demonstrate that SA/B-Uio-66 (Ce) exhibits favorable biocompatibility and potential for biomedical applications at both cellular and tissue levels.

Promoting MRSA-infected wound healing

Given the superior biocompatibility and desirable antibiofilm activity of SA/B-Uio-66 (Ce) against MRSA in vitro, we further evaluated its biofilm eradication efficacy in vivo using an MRSA-infected mouse excisional wound model (Fig. 7A). The infection model was established by inoculating 100 μL of 10^8 CFU/mL MRSA at the full-thickness wound site, followed by a 24-h incubation period to facilitate biofilm formation. The wounds were then treated with various antibacterial agents, with vancomycin (Van) serving as a positive control. After 24 h of treatment, the tissues at the wound sites were homogenized, and the bacteria were re-cultured to assess the impact of each treatment on early bacterial infection. As shown in Fig. 7B and C, the number of viable bacteria in the SA/B-Uio-66 (Ce) group was significantly reduced, with bacterial viability comparable to that of the Van treatment group. The antibacterial effect was significantly superior to that of amoxicillin (AM) and other treatment groups, indicating that SA/B-Uio-66 (Ce) can overcome MRSA resistance and effectively reduce bacterial load in wounds. To comprehensively assess cytocompatibility, body weight, and wound area were recorded and measured every two days, with associated recovery conditions calculated. As illustrated in Fig. 7D, the weight curves indicate that all groups maintained consistent growth throughout the study period. Wound healing status was documented photographically every two days, with the relevant observations during the 12-day period shown in Fig. 7E. During the first three days, no substantial differences were observed among the wound areas of all groups. However, from day 3 onwards, mice treated with SA/B-Uio-66 (Ce) and Van exhibited accelerated healing processes, with wound areas significantly smaller than those in the other groups, most notably on day 12. Importantly, no significant differences in wound healing were observed among the Uio-66 (Ce), B-Uio-66 (Ce), and SA groups (Fig. 7E, F).In summary, these results demonstrate that SA/B-Uio-66 (Ce) possesses potent bactericidal efficacy, promoting rapid wound healing.

On the twelfth day of the experiment, all mice were sacrificed, and the affected lesion tissues were collected for histological and molecular biological analysis. Hematoxylin−eosin (H&E) staining was first performed on the wound and surrounding areas, revealing histologically relevant indicators of wound healing, such as re-epithelialization and granulation tissue (Fig. 7G). Compared to the control, SA, and AM groups, the granulation tissue width (measured as the distance between the black dashed lines) was significantly reduced in the Uio-66 (Ce), B-Uio-66 (Ce), and Van groups. Notably, granulation tissue width was nearly absent in the SA/B-Uio-66 (Ce) group, consistent with the quantitative analysis of

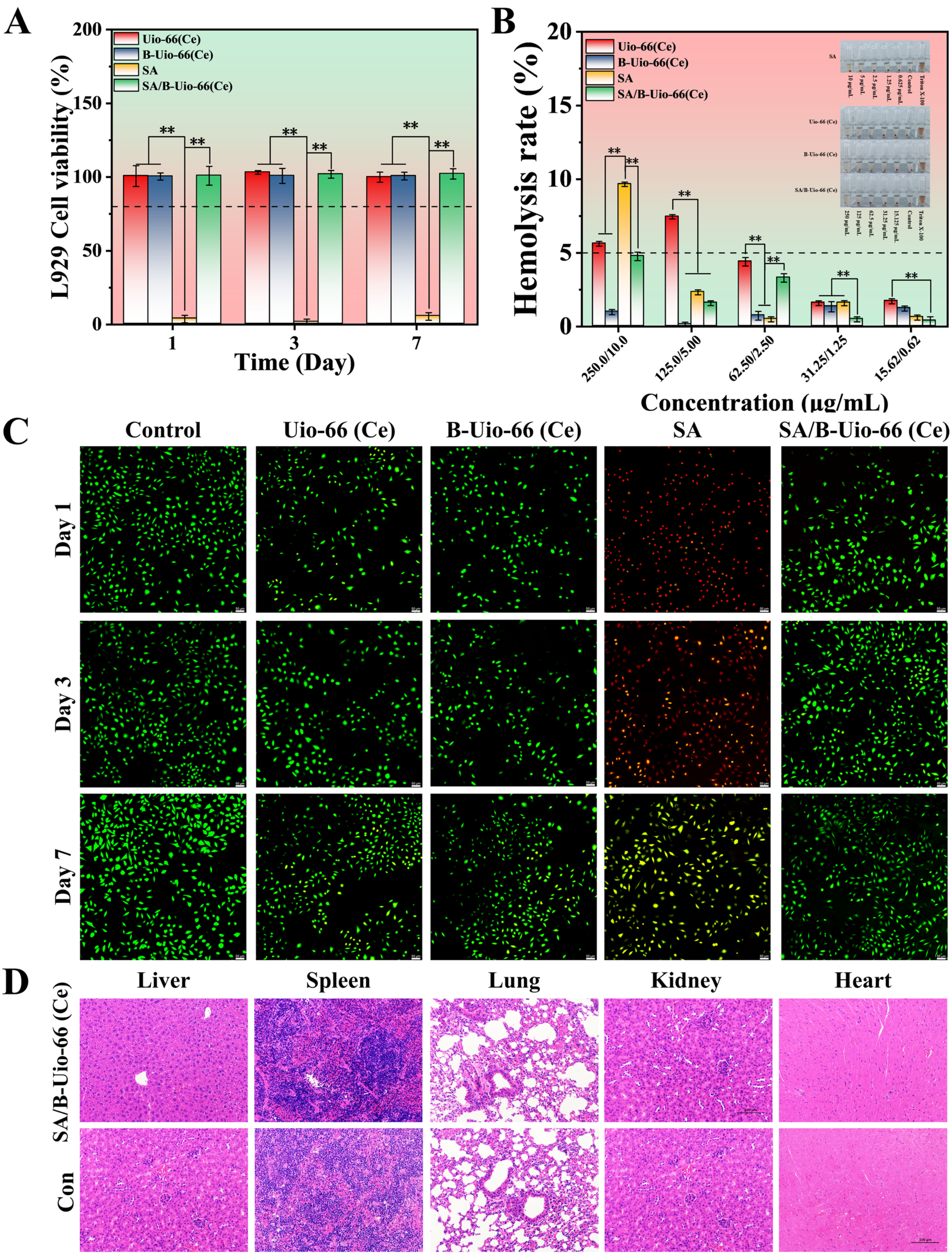

Fig. 6 In vitro and vivo biocompatibility assessment of SA/B-Uio-66 (Ce). **A** Cell viability of L929 cells after treatment at different times. **B** Percent hemolysis rate of different nanozymes. **C** The co-staining of Calcein and PI in L929 cell. **D** H&E sections of major organs (the heart, liver, spleen, lungs, and kidneys) of mice in different groups after 24 h treatment

wound area. Abnormal thickening of the newly formed epithelium and disordered arrangement of basal layer cells were observed at the wound edges in the control, SA, and AM groups (indicated by the blue dashed line in Fig. 7G). This condition improved progressively in the Uio-66 (Ce) and B-Uio-66 (Ce) groups, with the smoothest and flattest epithelium noted in the SA/B-Uio-66 (Ce) group, even surpassing that of the Van group. Additionally, we observed infiltration of blood cells and inflammatory cells in the central area of the wounds (highlighted in the red dashed box of Fig. 7G) and within the subepithelial layer (shown in the green dashed box of Fig. 7G), indicating subepithelial bleeding and persistent inflammation in the control, SA, and AM groups. However, these phenomena diminished in the B-Uio-66 (Ce) and SA/B-Uio-66 (Ce) groups, where new hair follicles were evident. Mice in these groups also displayed robust tissue restoration, characterized by smaller scar tissue areas and reduced neutrophil infiltration.

To specifically assess collagen formation and fiber arrangement in the wounded areas of newborn skin tissue, Masson's trichrome staining was conducted, as illustrated in Fig. 7H. The collagen fibrils were sparsely distributed in the control, SA, and AM groups, while collagen fibrils and dermal layers were prominently present in the SA/B-Uio-66 (Ce) group. Quantitative analysis of collagen deposition, shown in Fig. 7I, corroborated these findings, revealing that the SA/B-Uio-66 (Ce) group had the highest collagen deposition levels. To visualize vascularization within the wound bed, we employed CD31 immunohistochemical labeling to detect blood vessels in the wound sections and quantified vessel density using the digital image analysis tools in ImageJ software (Fig. 8A, B). The results indicated that the SA/B-Uio-66 (Ce) group exhibited the highest CD31 expression (stained brown). Macrophages are crucial to the inflammatory process of wound healing, with their activation and polarization being essential for initiating proliferation. However, a disorder in macrophage polarization from a pro-inflammatory (M1) to an anti-inflammatory (M2) phenotype can exacerbate infected wounds. On day 12, the SA/B-Uio-66 (Ce) group displayed a decrease in M1 macrophages (iNOS+) and an increase in the infiltration and distribution of M2 macrophages (CD206+) (Fig. 8C, D), suggesting that SA/B-Uio-66 (Ce) facilitates the shift in macrophage phenotype from M1 to M2. To further investigate the inhibitory effects of SA/B-Uio-66 (Ce) on the inflammatory response, we employed immunohistochemical staining to quantify the levels of representative inflammatory cytokines in the healing wound tissue (Fig. S17). The results revealed that the levels of inflammatory cytokines, such as TNF-α and IL-6, were significantly elevated in the control group, while the levels of anti-inflammatory cytokines, including IL-4 and IL-13, were markedly reduced. In contrast, the treatment groups exhibited a decrease in inflammatory cytokines and an increase in anti-inflammatory cytokines. Notably, the SA/B-Uio-66 (Ce) group demonstrated the most significant reduction in inflammatory cytokines, such as IL-6 and TNF-α, along with the highest levels of anti-inflammatory cytokines, including IL-4 and IL-13, observed on day 12. These findings indicate that the control group experienced excessive inflammation due to MRSA infection, whereas treatment with SA/B-Uio-66 (Ce) effectively mitigated the inflammatory response associated with infected wounds, resulting in the least inflammatory response among the treatment groups. This enhanced anti-inflammatory effect of SA/B-Uio-66 (Ce) likely facilitated macrophage polarization, angiogenesis, and collagen deposition, and ultimately contributed to improved wound healing [69].

Overall, these results confirm that SA/B-Uio-66 (Ce) plays a significant role in modulating the microenvironment of MRSA-infected wounds, showcasing excellent antibacterial properties, promoting epithelial regeneration and collagen deposition, inducing macrophage polarization, and enhancing angiogenesis (Fig. 8E). To address the practical requirements of clinical applications, we further fabricate microneedles by hyaluronic acid methacryloyl (HAMA, source from Yongqinquan Intelligent Equipment Co.Ltd, Suzhou, China) solution with SA/B-Uio-66 (Ce) (Fig. S18A) [70]. The force–displacement curve indicates that the addition of SA/B-Uio-66 (Ce) enhances the structural strength of the composite microneedles, with a yield strength meeting the minimum insertion force of 0.098 N/needle required to penetrate the skin barrier (Fig. S16B) [44]. Scanning electron microscopy results reveal a needle height of approximately 620 μm (Fig. S16E), enabling effective penetration of the stratum corneum for the treatment

(See figure on next page.)

Fig. 7 In vivo bacterial elimination and wound healing. **A** Animal experiment processes are depicted schematically. **B** MRSA colonies from in vivo tissue fluid after culturing with its corresponding real images. **C** Quantitative bacterial viability rates based on CFUs on day 1 after different treatments. **D** Mice weight curves throughout the skin regeneration procedure (n = 5). **E** Images of the addressed skin wounds: captured by time (The first day of therapy is referred to as Day 0). **F** Percentage of wound closure on mice after various treatments for 12 days. **G** H&E staining and **H** Masson staining images of the epidermal histological sections in different groups after 12 days. **I** Calculated collagen volume fraction value in (**H**)

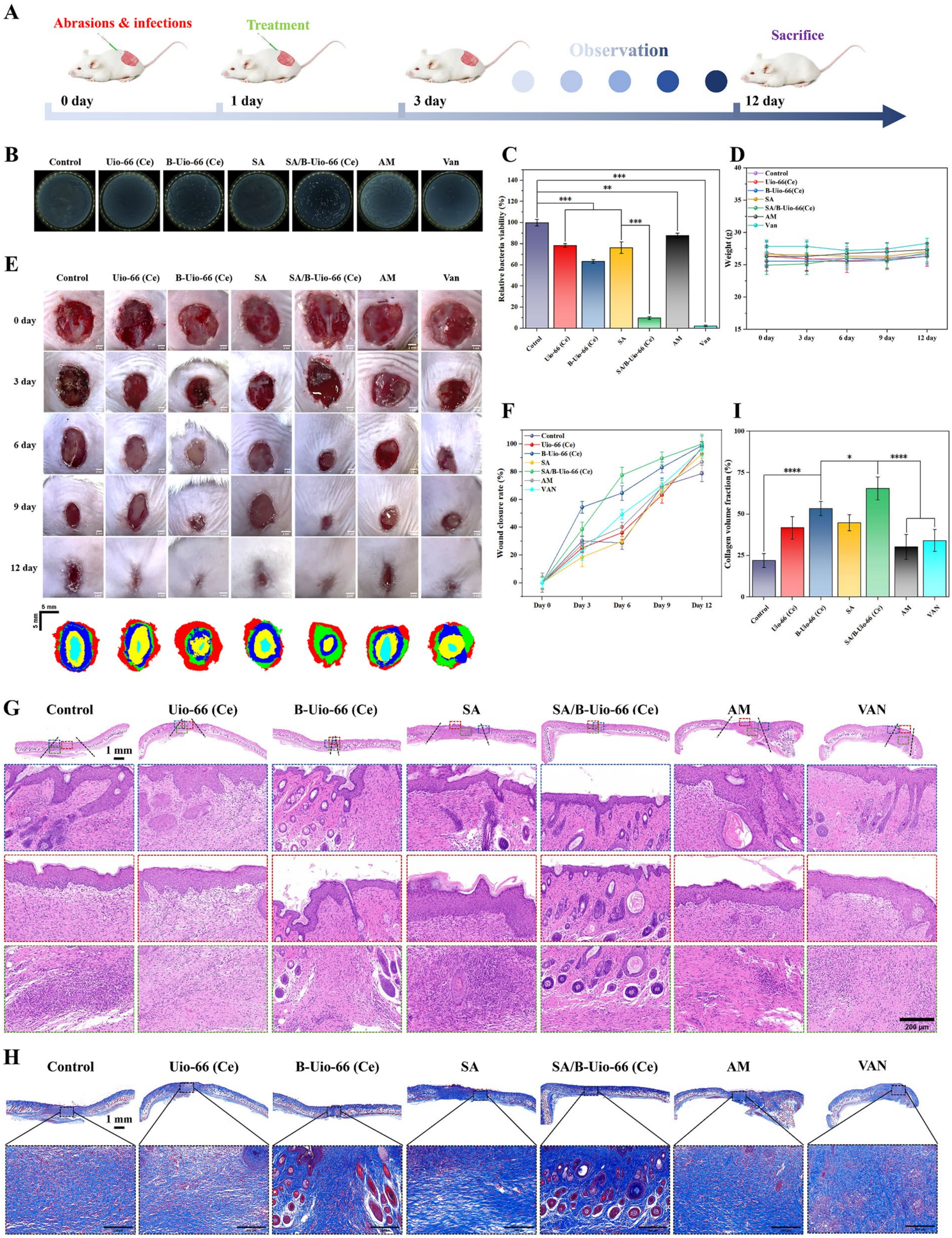

Fig. 7 (See legend on previous page.)

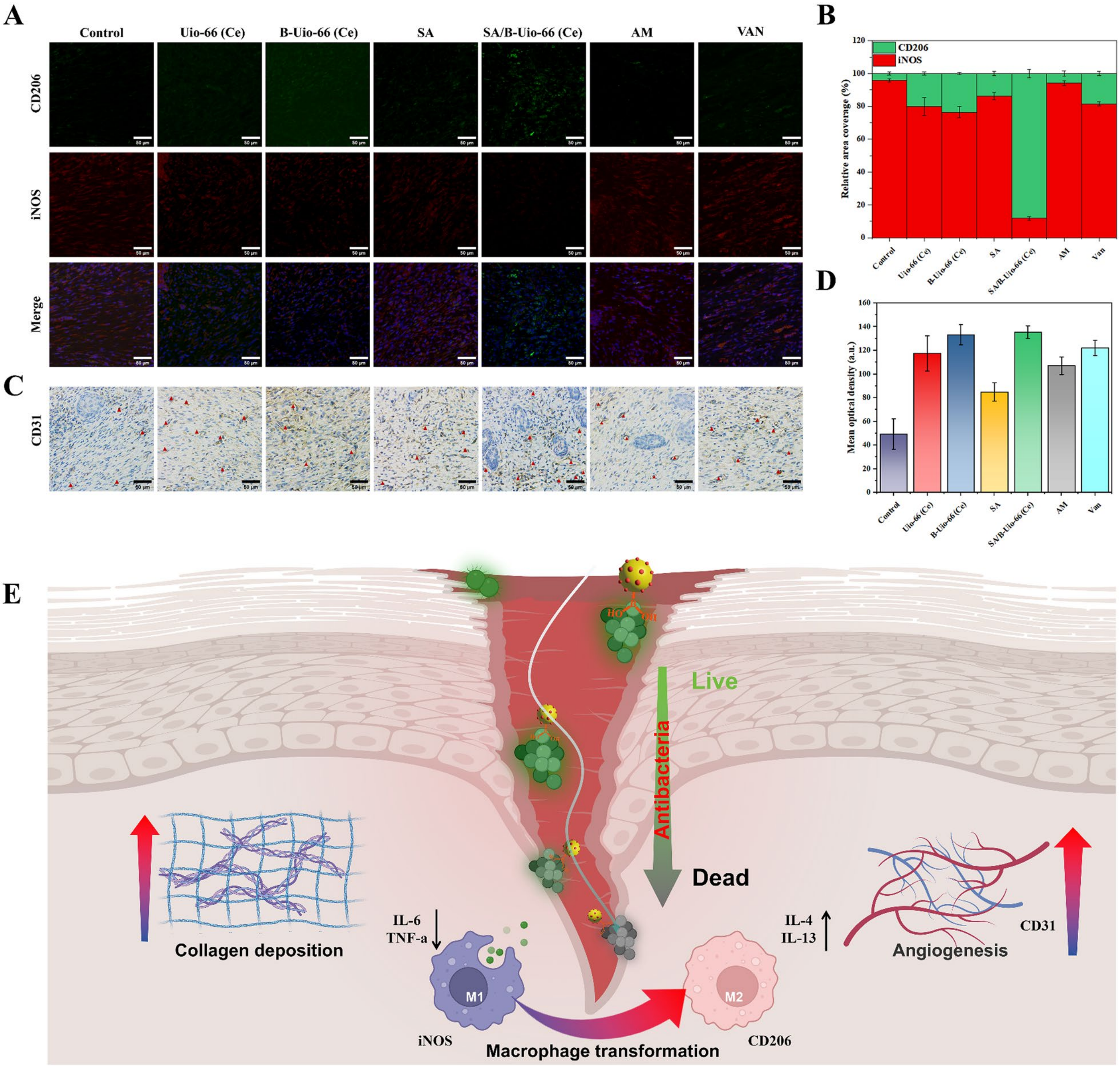

Fig. 8 **A** IF staining of iNOS and CD206 of infected wounds in different groups. **B** Quantification of the ratio of M2 to M1 macrophage. **C** IHC staining of CD31 of infected wounds in different groups. Red triangles indicate areas of vascular enrichment. **D** Quantification of vessel density. **E** Schematic diagram of the infected wound repair process

of subcutaneous bacterial infections, thereby providing a viable formulation strategy for CDT/chemotherapy systems.

Conclusion

In summary, we have designed and constructed a multi-enzyme activity cerium-based MOF to function as a CDT system for loading SA. This system is aimed at controlled regulating ROS and targeting MRSA to synergistically eradicate antibiotic-resistant biofilms and facilitate the repair of infected wounds. Leveraging the targeted modification of boric acid, the abundant cerium active catalytic sites within the porous structure, and the excellent antibacterial properties of SA, the synthesized cerium-based composite effectively achieves simultaneous biofilm destruction, EPS penetration, and enhanced BME adaptive ROS generation. Systematic in vitro studies demonstrate that the SA/B-Uio-66 (Ce) composite effectively targets

MRSA, facilitating in situ delivery of ROS and SA, thereby enhancing biofilm eradication. Moreover, transcriptomic analyses indicate that the accumulation of SA/B-Uio-66 (Ce) disrupts the cellular environment, interferes with energy metabolism, hinders bacterial attachment to EPS, and promotes the dispersion and eradication of biofilms by affecting genes associated with drug resistance, biosynthesis, and the preservation of both intra- and extracellular environments. Our in vivo investigations confirm that this system can effectively eradicate MRSA biofilms and expedite wound healing, exhibiting therapeutic efficacy comparable to vancomycin. We anticipate that the design of this CDT/chemotherapy system, characterized by its synergistic penetration, eradication capabilities, and pronounced ROS-catalytic activity, will not only provide a promising approach for treating antibiotic-resistant biofilm-induced recalcitrant infected wounds but also open new avenues for the detoxification and enhancement of natural pharmaceuticals.

Supplementary Information

The online version contains supplementary material available at https://doi.org/10.1186/s12951-025-03349-3.

Supplementary Material 1.

Acknowledgements

The authors would like to acknowledge critical and quantity of testing work supported by Beijing Zhongke Baice Testing Technology Service Co., Ltd. All authors discussed the results and commented on the manuscript. Further, we would like to acknowledge BioRender.com that was used to create parts of the figures.

Author contributions

Shiqi Chen and Haiyang Jiang conceived the idea and designed the project. Shiqi Chen and Yifan Li performed the experiments and analyzed the results. Qiang Ma, Jiayi Liang and Ke Han performed the transcriptomic analysis. Boyan Sun, Shuai Zhang and Zhiyue Feng. assisted with the figure production and experimental design. Shiqi Chen and Yifan Li wrote the manuscript. Sihan Wang, Hongping Wang and Haiyang Jiang. corrected the manuscript. Haiyang Jiang supervised the whole project.

Funding

This work was supported by the National Natural Science Foundation of China [Nos. 32373096].

Availability of data and materials

The data that support the findings of this study are available from the corresponding author upon reasonable request.

Declarations

Ethics approval and consent to participate

This study received approval from the Ethics Committee of China agricultural university, Beijing, China (AW32704202-2-15).

Consent for publication

All authors have approved the manuscript and agree for the submission.

Competing interests

The authors declare no competing interests.

Author details

[1] Department of Veterinary Pharmacology and Toxicology, National Key Laboratory of Veterinary Public Health Security, China Agricultural University, Beijing 100193, China. [2] NMPA Key Laboratory for Quality Control and Evaluation of Vaccines and Biological Products, SiChuan Institute of Musk Deer Breeding, SiChuan Institute for Drug Control (Sichuan Testing Center of Medical Devices), Chengdu 611731, China. [3] Department of Chemistry, Waterloo Institute for Nanotechnology, University of Waterloo, Waterloo, ON N2L 3G1, Canada.

Received: 24 January 2025 Accepted: 23 March 2025

References

1. Cao C, Zhang T, Yang N, Niu X, Zhou Z, Wang J, Yang D, Chen P, Zhong L, Dong X, Zhao Y. POD nanozyme optimized by charge separation engineering for light/pH activated bacteria catalytic/photodynamic therapy. Signal Transduct Target Ther. 2022;7(1):86. https://doi.org/10.1038/s41392-022-00900-8.
2. Lubkin A, Lee WL, Alonzo F, Wang C, Aligo J, Keller M, Girgis NM, Reyes-Robles T, Chan R, Malley AO, Buckley P, Vozhilla N, Vasquez MT, Su J, Sugiyama M, Yeung ST, Coffre M, Bajwa S, Chen E, Martin P, Kim SY, Loomis C, Worthen GS, Shopsin B, Khanna KM, Weinstock D, Lynch AS, Koralov SB, Loke P, Cadwell K, Torres VJ. Staphylococcus aureus leukocidins target endothelial DARC to cause lethality in mice. Cell Host Microbe. 2019;25(3):463–70. https://doi.org/10.1016/j.chom.2019.01.015.
3. Hemmige V, Arias CA, Pasalar S, Giordano TP. Skin and soft tissue infection in people living with human immunodeficiency virus in a large, urban, public healthcare system in Houston, Texas, 2009–2014. Clin Infect Dis. 2020;70(9):1985–92. https://doi.org/10.1093/cid/ciz509.
4. Yu Y, Li P, Zhu C, Ning N, Zhang S, Vancso GJ. Multifunctional and recyclable photothermally responsive cryogels as efficient platforms for wound healing. Adv Funct Mater. 2019;29(35):1904402. https://doi.org/10.1002/adfm.201904402.
5. Li K, Li D, Li C, Zhuang P, Dai C, Hu X, Wang D, Liu Y, Mei X, Rotello VM. Efficient in vivo wound healing using noble metal nanoclusters. Nanoscale. 2021;13(13):6531–7. https://doi.org/10.1039/d0nr07176e.
6. Li K, Li D, Li C, Zhuang P, Dai C, Hu X, Wang D, Liu Y, Mei X, Rotello VM. Retracted article: efficient wound healing using noble metal nanoclusters. Nanoscale. 2021;13(13):6531–7. https://doi.org/10.1039/d0nr07176e.
7. Kinney KJ, Tang SS, Wu X, Tran PM, Bharadwaj NS, Gibson-Corley KN, Forsythe AN, Kulhankova K, Gumperz JE, Salgado-Pabón W. Sec is an antiangiogenic virulence factor that promotes staphylococcus aureus endocarditis independent of superantigen activity. Sci Adv. 2022;8(19):o1072. https://doi.org/10.1126/sciadv.abo1072.
8. Xiao S, Xie L, Gao Y, Wang M, Geng W, Wu X, Rodriguez RD, Cheng L, Qiu L, Cheng C. Artificial phages with biocatalytic spikes for synergistically eradicating antibiotic-resistant biofilms. Adv Mater. 2024;36(32):2404411. https://doi.org/10.1002/adma.202404411.
9. Buzzo JR, Devaraj A, Gloag ES, Jurcisek JA, Robledo-Avila F, Kesler T, Wilbanks K, Mashburn-Warren L, Balu S, Wickham J, Novotny LA, Stoodley P, Bakaletz LO, Goodman SD. Z-form extracellular DNA is a structural component of the bacterial biofilm matrix. Cell. 2021;184(23):5740–58. https://doi.org/10.1016/j.cell.2021.10.010.
10. Yu S, Su T, Wu H, Liu S, Wang D, Zhao T, Jin Z, Du W, Zhu M, Chua SL, Yang L, Zhu D, Gu L, Ma LZ. PsLG, a self-produced glycosyl hydrolase, triggers biofilm disassembly by disrupting exopolysaccharide matrix. Cell Res. 2015;25(12):1352–67. https://doi.org/10.1038/cr.2015.129.
11. Karygianni L, Ren Z, Koo H, Thurnheer T. Biofilm matrixome: extracellular components in structured microbial communities. Trends Microbiol. 2020;28(8):668–81. https://doi.org/10.1016/j.tim.2020.03.016.
12. Ghosh S, Sinha M, Samanta R, Sadhasivam S, Bhattacharyya A, Nandy A, Saini S, Tandon N, Singh H, Gupta S, Chauhan A, Aavula KK, Varghese SS, Shi P, Ghosh S, Garg MK, Saha T, Padhye A, Ghosh S, Jang HL, Sengupta S. A potent antibiotic-loaded bone-cement implant against staphylococcal

bone infections. Nat Biomed Eng. 2022;6(10):1180–95. https://doi.org/10.1038/s41551-022-00950-x.

13. Zhang C, Bu W, Ni D, Zhang S, Li Q, Yao Z, Zhang J, Yao H, Wang Z, Shi J. Synthesis of iron nanometallic glasses and their application in cancer therapy by a localized Fenton reaction. Angew Chem. 2016;55(6):2101–6. https://doi.org/10.1002/anie.201510031.
14. Fu L, Zhang W, Zhou X, Fu J, He C. Tumor cell membrane-camouflaged responsive nanoparticles enable MRI-guided immuno-chemodynamic therapy of orthotopic osteosarcoma. Bioact Mater. 2022;17:221–33. https://doi.org/10.1016/j.bioactmat.2022.01.035.
15. Dai W, Shu R, Yang F, Li B, Johnson HM, Yu S, Yang H, Chan YK, Yang W, Bai D, Deng Y. Engineered bio-heterojunction confers extra- and intracellular bacterial ferroptosis and hunger-triggered cell protection for diabetic wound repair. Adv Mater. 2024;36(9):2305277. https://doi.org/10.1002/adma.202305277.
16. Guo Y, Ding S, Shang C, Zhang C, Li M, Zhang Q, Gu L, Heng BC, Zhang S, Mei F, Huang Y, Zhang X, Xu M, Jiang J, Guo S, Deng X, Chen L. Multifunctional PtCuTe nanosheets with strong ROS scavenging and ROS-independent antibacterial properties promote diabetic wound healing. Adv Mater. 2024;36(8):2306292. https://doi.org/10.1002/adma.202306292.
17. Lu C, Zhang C, Wang P, Zhao Y, Yang Y, Wang Y, Yuan H, Qu S, Zhang X, Song G, Pu K. Light-free generation of singlet oxygen through manganese-thiophene nanosystems for pH-responsive chemiluminescence imaging and tumor therapy. Chem. 2020;6(9):2314–34. https://doi.org/10.1016/j.chempr.2020.06.024.
18. Wu Y, Xu W, Jiao L, Tang Y, Chen Y, Gu W, Zhu C. Defect engineering in nanozymes. Mater Today. 2022;52:327–47. https://doi.org/10.1016/j.mattod.2021.10.032.
19. Zhang X, Li G, Chen G, Wu D, Wu Y, James TD. Enzyme mimics for engineered biomimetic cascade nanoreactors: mechanism, applications, and prospects. Adv Funct Mater. 2021;31(50):2106139. https://doi.org/10.1002/adfm.202106139.
20. Ghosh S, Roy P, Karmodak N, Jemmis ED, Mugesh G. Nanoisozymes: crystal-facet-dependent enzyme-mimetic activity of v2o5 nanomaterials. Angew Chem Int Ed. 2018;57(17):4510–5. https://doi.org/10.1002/anie.201800681.
21. Gao F, Shao T, Yu Y, Xiong Y, Yang L. Surface-bound reactive oxygen species generating nanozymes for selective antibacterial action. Nat Commun. 2021. https://doi.org/10.1038/s41467-021-20965-3.
22. Liu Y, Li Z, Fan F, Zhu X, Jia L, Chen M, Du P, Yang L, Yang S. Boosting antitumor sonodynamic therapy efficacy of black phosphorus via covalent functionalization. Adv Sci. 2021;8(20):2102422. https://doi.org/10.1002/advs.202102422.
23. Bayer U, Werner D, Maichle Mössmer C, Anwander R. Effective and reversible carbon dioxide insertion into cerium pyrazolates. Angew Chem. 2020;59(14):5830–6. https://doi.org/10.1002/anie.201916483.
24. Jiang Y, Chen Z, Sui N, Zhu Z. Data-driven evolutionary design of multienzyme-like nanozymes. J Am Chem Soc. 2024;146(11):7565–74. https://doi.org/10.1021/jacs.3c13588.
25. Han L, Zhang Y, Huang B, Bian X, Tang BZ. Aggregation-induced emission artificial enzyme (AIEzyme) with DNase-like activity: imaging and matrix cleavage for combating bacterial biofilm. Aggregate. 2023;4(5): e360. https://doi.org/10.1002/agt2.360.
26. Yuan X, Xiong J, Wu X, Ta N, Liu S, Li Z, Lou W. Ultrasmall Ce-based metal–organic frameworks nanozyme with hydrolytic activity for boosting antibiofilm therapy. Chem Eng J. 2024;480:148246. https://doi.org/10.1016/j.cej.2023.148246.
27. Liu Z, Wang F, Ren J, Qu X. A series of MOF/Ce-based nanozymes with dual enzyme-like activity disrupting biofilms and hindering recolonization of bacteria. Biomaterials. 2019;208:21–31. https://doi.org/10.1016/j.biomaterials.2019.04.007.
28. Komiyama M. Ce-based solid-phase catalysts for phosphate hydrolysis as new tools for next-generation nanoarchitectonics. Sci Technol Adv Mater. 2023;24(1):2250705. https://doi.org/10.1080/14686996.2023.2250705.
29. Chen L, Ye J, Yang Y, Yin P, Feng H, Chen C, Zhang X, Wei M, Truhlar DG. Catalytic conversion furfuryl alcohol to tetrahydrofurfuryl alcohol and 2-methylfuran at terrace, step, and corner sites on ni. Acs Catal. 2020;10(13):7240–9. https://doi.org/10.1021/acscatal.0c01441.
30. Zhang L, Wang H, Qu X. Biosystem-inspired engineering of nanozymes for biomedical applications. Adv Mater. 2024;36(10):2211147. https://doi.org/10.1002/adma.202211147.
31. Wang X, Hu W, Xia XH, Wang C. Implanting of single zinc sites into 2D metal–organic framework nanozymes for boosted antibiofilm therapy. Adv Funct Mater. 2023;33(10):2212798. https://doi.org/10.1002/adfm.202212798.
32. Sealy C. Ruthenium-based MOF scavenges reactive species to tackle inflammation. Nano Today. 2022;47:101680. https://doi.org/10.1016/j.nantod.2022.101680.
33. Zheng L, Wang F, Jiang C, Ye S, Tong J, Dramou P, He H. Recent progress in the construction and applications of metal-organic frameworks and covalent-organic frameworks-based nanozymes. Coord Chem Rev. 2022;471:214760. https://doi.org/10.1016/j.ccr.2022.214760.
34. Tang Y, Han Y, Zhao J, Lv Y, Fan C, Zheng L, Zhang Z, Liu Z, Li C, Lin Y. A rational design of metal–organic framework nanozyme with high-performance copper active centers for alleviating chemical corneal burns. Nano-Micro Lett. 2023;15(1):112. https://doi.org/10.1007/s40820-023-01059-9.
35. Lammert M, Wharmby MT, Smolders S, Bueken B, Lieb A, Lomachenko KA, Vos DD, Stock N. Cerium-based metal organic frameworks with UiO-66 architecture: synthesis, properties and redox catalytic activity. Chem Commun. 2015;51(63):12578–81. https://doi.org/10.1039/c5cc02606g.
36. Shan J, Du L, Wang X, Zhang S, Li Y, Xue S, Tang Q, Liu P. Ultrasound trigger Ce-based MOF nanoenzyme for efficient thrombolytic therapy. Adv Sci. 2024;11(20):2304441. https://doi.org/10.1002/advs.202304441.
37. Chen Z, Song S, Zeng H, Ge Z, Liu B, Fan Z. 3D printing MOF nanozyme hydrogel with dual enzymatic activities and visualized glucose monitoring for diabetic wound healing. Chem Eng J. 2023;471:144649. https://doi.org/10.1016/j.cej.2023.144649.
38. Wang Z, Lu J, Yuan Z, Pi W, Huang X, Lin X, Zhang Y, Lei H, Wang P. Natural carrier-free binary small molecule self-assembled hydrogel synergize antibacterial effects and promote wound healing by inhibiting virulence factors and alleviating the inflammatory response. Small. 2023;19(5):2205528. https://doi.org/10.1002/smll.202205528.
39. Huang L, Lan J, Wang J, Huang H, Lu K, Zhou Z, Xin S, Zhang Z, Wang J, Dai P, Chen X, Hou W. Bioactivity and mechanism of action of sanguinarine and its derivatives in the past 10 years. Biomed Pharmacother. 2024;173:116406. https://doi.org/10.1016/j.biopha.2024.116406.
40. Chen M, Zhang J, Qi J, Dong R, Liu H, Wu D, Shao H, Jiang X. Boronic acid-decorated multivariate photosensitive metal–organic frameworks for combating multi-drug-resistant bacteria. ACS Nano. 2022;16(5):7732–44. https://doi.org/10.1021/acsnano.1c11613.
41. Tang H, Chu W, Xiong J, Wu H, Cheng L, Cheng L, Luo J, Yin H, Li J, Li J, Yang J, Li J. Seeking cells, targeting bacteria: a cascade-targeting bacteria-responsive nanosystem for combating intracellular bacterial infections. Small. 2024. https://doi.org/10.1002/smll.202311967.
42. Xiao J, Guo Z, Lv G, Yan Z, Liu T, Wang Y, Liu H, Martínez J, Yin L, Liu X, Jiang H, Weizmann Y, Wang X. Neutrophil extracellular traps-inspired bismuth-based polypeptide nanonets for synergetic treatment of bacterial infections. Adv Healthc Mater. 2024. https://doi.org/10.1002/adhm.202401993.
43. Rego RM, Sriram G, Ajeya KV, Jung H, Kurkuri MD, Kigga M. Cerium based uio-66 MOF as a multipollutant adsorbent for universal water purification. J Hazard Mater. 2021;416:125941. https://doi.org/10.1016/j.jhazmat.2021.125941.
44. Sun Y, Liu M, Sun W, Tang X, Zhou Y, Zhang J, Yang B. A hemoglobin bionics-based system for combating antibiotic resistance in chronic diabetic wounds via iron homeostasis regulation. Adv Mater. 2024;36(30):2405002. https://doi.org/10.1002/adma.202405002.
45. Geng C, He S, Yu S, Johnson HM, Shi H, Chen Y, Chan YK, He W, Qin M, Li X, Deng Y. Achieving clearance of drug-resistant bacterial infection and rapid cutaneous wound regeneration using an ROS-balancing-engineered heterojunction. Adv Mater. 2024;36(16):2310599. https://doi.org/10.1002/adma.202310599.
46. Li K, Yang J, Gu J. Salting-in species induced self-assembly of stable MOFs. Chem Sci. 2019;1(22):5743–8. https://doi.org/10.1039/c9sc01447k.
47. Jiang B, Duan D, Gao L, Zhou M, Fan K, Tang Y, Xi J, Bi Y, Tong Z, Gao GF, Xie N, Tang A, Nie G, Liang M, Yan X. Standardized assays for determining the catalytic activity and kinetics of peroxidase-like nanozymes. Nat Protoc. 2018;13(7):1506–20. https://doi.org/10.1038/s41596-018-0001-1.
48. Zou W, Ye C, Wang Y, Li W, Huang X. A hybrid ratiometric probe for glucose detection based on synchronous responses to fluorescence quenching and resonance light scattering enhancement of boronic acid

functionalized carbon dots. Sens Actuators B Chem. 2018;271:54–63. https://doi.org/10.1016/j.snb.2018.05.115.
49. Wang Q, Kaminska I, Niedziolka-Jonsson J, Opallo M, Li M, Boukherroub R, Szunerits S. Sensitive sugar detection using 4-aminophenylboronic acid modified graphene. Biosens Bioelectron. 2013;50:331–7. https://doi.org/10.1016/j.bios.2013.06.015.
50. Bello A, Bergmann U, Vepsäläinen J, Leiviskä T. Effects of tree harvesting time and tannin cold/hot-water extraction procedures on the performance of spruce tannin biocoagulant for water treatment. Chem Eng J. 2022;449:137809. https://doi.org/10.1016/j.cej.2022.137809.
51. Chen X, He Q, Zhai Q, Tang H, Li D, Zhu X, Zheng X, Jian G, Cannon RD, Mei L, Wang S, Ji P, Song J, Chen T. Adaptive nanoparticle-mediated modulation of mitochondrial homeostasis and inflammation to enhance infected bone defect healing. ACS Nano. 2023;17(22):22960–78. https://doi.org/10.1021/acsnano.3c08165.
52. Li L, Cao S, Wu Z, Guo R, Xie L, Wang L, Tang Y, Li Q, Luo X, Ma L, Cheng C, Qiu L. Modulating electron transfer in vanadium-based artificial enzymes for enhanced ROS-catalysis and disinfection. Adv Mater. 2022;34(17):2108646. https://doi.org/10.1002/adma.202270128.
53. Huang Y, Ren J, Qu X. Nanozymes: classification, catalytic mechanisms, activity regulation, and applications. Chem Rev. 2019;119(6):4357–412. https://doi.org/10.1021/acs.chemrev.8b00672.
54. Koo H, Allan RN, Howlin RP, Stoodley P, Hall-Stoodley L. Targeting microbial biofilms: current and prospective therapeutic strategies. Nat Rev Microbiol. 2017;15(12):740–55. https://doi.org/10.1038/nrmicro.2017.99.
55. Peng H, Rossetto D, Mansy SS, Jordan MC, Roos KP, Chen IA. Treatment of wound infections in a mouse model using Zn^{2+} -releasing phage bound to gold nanorods. ACS Nano. 2022;16(3):4756–74. https://doi.org/10.1021/acsnano.2c00048.
56. Lin S, Li X, Zhang W, Shu G, Tolker-Nielsen T, Li H, Xu F, Lin J, Peng G, Zhang L, Fu H. Enhanced penetration and biofilm eradication by sophorolipid micelles encapsulating Honokiol: a comprehensive solution for biofilm-associated lung infections. J Nanobiotechnol. 2025;23(1):16–76. https://doi.org/10.1186/s12951-025-03144-0.
57. Liu Z, Guo K, Yan L, Zhang K, Wang Y, Ding X, Zhao N, Xu F. Janus nanoparticles targeting extracellular polymeric substance achieve flexible elimination of drug-resistant biofilms. Nat Commun. 2023;14(1):5132. https://doi.org/10.1038/s41467-023-40830-9.
58. Sun J, Rutherford ST, Silhavy TJ, Huang KC. Physical properties of the bacterial outer membrane. Nat Rev Microbiol. 2022;20(4):236–48. https://doi.org/10.1038/s41579-021-00638-0.
59. Rees DC, Johnson E, Lewinson O. ABC transporters: the power to change. Nat Rev Mol Cell Biol. 2009;10(3):218–27. https://doi.org/10.1038/nrm2646.
60. Cho C, Kowalsky AH, Namkoong S, Park S, Wu S, Kim B, James A, Gu B, Semple IA, Tohamy MA, Solanki S, Cho U, Greenson JK, Shah YM, Kim M, Lee JH. Concurrent activation of growth factor and nutrient arms of mtorc1 induces oxidative liver injury. Cell Discov. 2019;5(1):1–18. https://doi.org/10.1038/s41421-019-0131-9.
61. Ezraty B, Gennaris A, Barras F, Collet J. Oxidative stress, protein damage and repair in bacteria. Nat Rev Microbiol. 2017;15(7):385–96. https://doi.org/10.1038/nrmicro.2017.26.
62. Gu Y, Dong J, Li J, Luo Q, Dong X, Tang G, Zhang J, Du X, Pu Q, He L, Zhao K, Han D, Xin J. Antibacterial activity and mechanism of sanguinarine against *Staphylococcus aureus* by interfering with the permeability of the cell wall and membrane and inducing bacterial ROS production. Front Vet Sci. 2023;10:1121082. https://doi.org/10.3389/fvets.2023.1121082.
63. Liu Z, Wang W, Zhang Z, Sun L, Wu S. Natural antibacterial and antivirulence alkaloids from *Macleaya cordata* against methicillin-resistant *Staphylococcus aureus*. Front Pharmacol. 2022;13:813172. https://doi.org/10.3389/fphar.2022.813172.
64. Qu Q, Huang X, Zhu Z, Wang J, Zhao M, Cui W, Zheng Y, Liu Y, Chen X, Zhang Z, Dong N, Dong C, Li Y. Targeting membrane integrity and imidazoleglycerol-phosphate dehydratase: sanguinarine multifaceted approach against staphylococcus aureus biofilms. Phytomedicine. 2025;138:156428. https://doi.org/10.1016/j.phymed.2025.156428.
65. Xie L, Wu H, Li Y, Shi L, Liu Y. Recent development of nanozymes for combating bacterial drug resistance: a review. Adv Healthc Mater. 2024. https://doi.org/10.1002/adhm.202402659.
66. Yang L, Pijuan-Galito S, Rho HS, Vasilevich AS, Eren AD, Ge L, Habibović P, Alexander MR, de Boer J, Carlier A, van Rijn P, Zhou Q. High-throughput methods in the discovery and study of biomaterials and materiobiology. Chem Rev. 2021;121(8):4561–677. https://doi.org/10.1021/acs.chemrev.0c00752.
67. Makvandi P, Wang CY, Zare EN, Borzacchiello A, Niu LN, Tay FR. Metal-based nanomaterials in biomedical applications: antimicrobial activity and cytotoxicity aspects. Adv Funct Mater. 2020;30(22):1910021. https://doi.org/10.1002/adfm.201910021.
68. Zhang X, Wang Z, Jiang H, Zeng H, An N, Liu B, Sun L, Fan Z. Self-powered enzyme-linked microneedle patch for scar-prevention healing of diabetic wounds. Sci Adv. 2023;9(28): h1415. https://doi.org/10.1126/sciadv.adh1415.
69. Liu C, Zeng H, Chen Z, Ge Z, Wang B, Liu B, Fan Z. Sprayable methacrylic anhydride-modified gelatin hydrogel combined with bionic neutrophils nanoparticles for scar-free wound healing of diabetes mellitus. Int J Biol Macromol. 2022;202:418–30. https://doi.org/10.1016/j.ijbiomac.2022.01.083.
70. Wang Z, Liang X, Wang G, Wang X, Chen Y. Emerging bioprinting for wound healing. Adv Mater. 2023. https://doi.org/10.1002/adma.202304738.

Publisher's Note